The Astrophysical Journal, 756:92 (15pp), 2012 September 1 doi:10.1088/0004-637X/756/1/92

THE NEAR-INFRARED BACKGROUND INTENSITY AND ANISOTROPIES DURING THE EPOCH OF REIONIZATION

Asantha Cooray[1], Yan Gong[1], Joseph Smidt[1], and Mario G. Santos[2]
[1] Department of Physics & Astronomy, University of California, Irvine, CA 92697, USA
[2] CENTRA, Instituto Superior Técnico, Technical University of Lisbon, Lisboa 1049-001, Portugal
Received 2012 May 9; accepted 2012 July 9; published 2012 August 20

ABSTRACT

A fraction of the extragalactic near-infrared (near-IR) background light involves redshifted photons from the ultraviolet (UV) emission from galaxies present during reionization at redshifts above 6. The absolute intensity and the anisotropies of the near-IR background provide an observational probe of the first-light galaxies and their spatial distribution. We estimate the extragalactic background light intensity during reionization by accounting for the stellar and nebular emission from first-light galaxies. We require the UV photon density from these galaxies to generate a reionization history that is consistent with the optical depth to electron scattering from cosmic microwave background measurements. We also require the bright-end luminosity function (LF) of galaxies in our models to reproduce the measured Lyman-dropout LFs at redshifts of 6–8. The absolute intensity is about 0.1–0.4 nW m^{-2} sr^{-1} at the peak of its spectrum at $\sim$1.1 μm. We also discuss the anisotropy power spectrum of the near-IR background using a halo model to describe the galaxy distribution. We compare our predictions for the anisotropy power spectrum to existing measurements from deep near-IR imaging data from *Spitzer*/IRAC, *Hubble*/NICMOS, and *AKARI*. The predicted rms fluctuations at tens of arcminute angular scales are roughly an order of magnitude smaller than the existing measurements. While strong arguments have been made that the measured fluctuations do not have an origin involving faint low-redshift galaxies, we find that measurements in the literature are also incompatible with galaxies present during the era of reionization. The measured near-IR background anisotropies remain unexplained with an unknown origin.

Key words: cosmology: theory – diffuse radiation – intergalactic medium – large-scale structure of universe

Online-only material: color figures

1. INTRODUCTION

The optical and UV radiation from sources present during reionization is expected to leave a signature in the extragalactic background light (EBL) at near-IR wavelengths (e.g., Santos et al. 2002; Salvaterra & Ferrara 2003; Cooray & Yoshida 2004; Fernandez & Komatsu 2006; Raue 2009). Such radiation is not expected to be present in the background light at UV and optical wavelengths due to the redshifted Lyman limit. The exact intensity from first-light galaxies present during reionization is currently unknown. The first predictions suggested an intensity as high as 10–30 nW m^{-2} sr^{-1} (Santos et al. 2002; Salvaterra & Ferrara 2003). These estimates were partly motivated by the need to explain the difference between DIRBE EBL measurements (e.g., Cambrésy et al. 2001) and the integrated galaxy light (IGL) from deep galaxy counts (Madau & Pozzetti 2000; Totani et al. 2001).

These predictions with high backgrounds were questioned by Madau & Silk (2005) based on existing limits related to metal content at high redshifts and the X-ray background produced by stellar end products such as black holes. They suggest an intensity less than about 2.5 nW m^{-2} sr^{-1} in the *J* band from a galaxy population made up of Population III (Pop III) stars during reionization (Madau & Silk 2005). With a combination of Population II (Pop II) stars and changes to the lifetime of stars, Fernandez & Komatsu (2006) argued that the background could be as high as 4–8 nW m^{-2} sr^{-1}. Even in such a scenario, a simple estimate of the UV photon density at $z > 6$ shows that there are roughly an order of magnitude higher number of H-ionizing photons per baryon during reionization than necessary to explain the reionization history. Since one does not expect more than a few H-ionizing photons per baryon during reionization, a first-order estimate suggests that the background intensity cannot be larger than a few tenths nW m^{-2} sr^{-1} between 1 and 2 μm.

Unfortunately, a direct search for the integrated intensity of galaxies present during reionization based on absolute background measurements has been problematic due to the confusion with the zodiacal foreground. At 1 AU, zodiacal light is two to three orders of magnitude brighter than the $\sim$10 nW m^{-2} sr^{-1} intensity produced by extragalactic sources. While challenging, techniques have been devised to estimate the zodiacal dust column density based on the line strengths of Fraunhofer lines seen in the dust-scattered solar spectrum (e.g., Bernstein & Dyson 2003). Instead of the absolute background, in Cooray et al. (2004; also Kashlinsky et al. 2004), it was proposed that the galaxies present during reionization can be studied with anisotropies of the near-IR background. The anisotropy studies have the potential to probe deeper than the absolute experiments and could study a galaxy population present during reionization that leads to an intensity well below 0.1 nW m^{-2} sr^{-1} (Cooray et al. 2004).

This suggestion has motivated experimental measurements on the near-IR anisotropy power spectrum with data from *Spitzer*/IRAC, *Hubble Space Telescope* (*HST*)/NICMOS, and *AKARI*. After a deep removal of point sources, Kashlinsky et al. (2005, 2007, 2012) claimed a detection of first-light galaxy fluctuations at $z > 8$. The detected signal is an excess of clustering power above shot noise on the largest angular scales. A similar suggestion was also made by an *AKARI* group (Matsumoto et al. 2011), but an analysis of the *HST*/NICMOS Ultra Deep Field led to an opposite conclusion that the sources

contributing to the near-IR excess fluctuations are at $z < 8$ (Thompson et al. 2007). Due to the limited areas of existing deep surveys, near-IR background anisotropy measurements are limited to angular scales less than about 1°. The limited field of view is especially a problem for existing NICMOS UDF measurements (Thompson et al. 2007), where the fluctuations are limited to angular scales less than 5′. Separately, a joint analysis of IRAC and *HST*/Advanced Camera for Surveys data in the same GOODS fields as studied by Kashlinsky et al. (2007) led to the suggestion that up to 50% of the excess fluctuations at 3.6 μm could come from faint dwarf galaxies at $z \sim 2$ (Cooray et al. 2007; Chary et al. 2008). Through detailed models combined with more recent measurements of faint galaxy clustering, Helgason et al. (2012) have lowered this low-redshift contribution to 3.6 μm intensity fluctuations to be at most 20%. The rest of the anisotropies continue to be interpreted as originating from first-light galaxies during reionization (Kashlinsky et al. 2012).

While there are still uncertainties on the exact intensity and the amplitude of intensity fluctuations in experimental measurements, the situation is no different on the theory side. The first estimates on the anisotropy power spectrum made use of linear theory clustering (Cooray et al. 2004). Fernandez et al. (2010) used numerical simulations of reionization to predict the expected power spectrum during reionization. Their power spectrum has a shape in the form of a power law with $C_l \propto l^{1/2}$ between 10 arcminute to arcsecond angular scales. Fernandez et al. (2010) suggested that the power-law behavior arises from significant nonlinear biasing of dark matter halos at high redshifts. Due to the limited box sizes of existing reionization simulations of the order 100–140 Mpc on the side, numerical studies are limited to angular scales of 30 arcmin and below at $z > 6$.

With the availability of WFC3 on the *HST*, dedicated IR background experiments (e.g., CIBER sounding-rocket experiment; Bock et al. 2006), and plans for a future space-based absolute intensity measurement (ZEBRA[3]; Cooray et al. 2009), there is now a clear need to revisit theoretical predictions on both the absolute intensity and the anisotropy power spectrum from galaxies present during reionization. While current multi-band *Spitzer* and *AKARI* measurements do not overlap in the same fields, the combination of IRAC and WFC3 data on some of the same well-studied fields on the sky (e.g., fields covered by the CANDELS survey; Grogin et al. 2011; Koekemoer et al. 2011) will soon allow the spectral energy distribution (SED) of intensity fluctuations be studied uniformly. Separately, CIBER is conducting spectral imaging absolute measurements between 0.8 and 1.6 μm in wide 4 deg^2 fields instantaneously using multiple sounding-rocket flights (Bock et al. 2012). The combination of IRAC and CIBER is capable of extending anisotropy measurements out to angular scales of more than a degree from optical to 4.5 μm.

In this work, we establish both the mean intensity and the anisotropy power spectrum of galaxies present during reionization. We update Cooray et al. (2004) by taking into account recent developments in the study of reionization, and by introducing a halo model to calculate the nonlinear clustering of the IR background intensity. The stellar and nebular emission from first-light galaxies follow the calculations presented in Fernandez & Komatsu (2006), but we specifically require that the UV photon background produced by the galaxy population present from $z \sim 6$ to 30 is consistent with the optical depth to electron scattering as measured by the *Wilkinson Microwave Anisotropy Probe* (*WMAP*) polarization data with a value of 0.088 ± 0.014 (Komatsu et al. 2011). We account for the current uncertainty in the optical depth by introducing variations to the fiducial model so that the optical depth to electron scattering varies between 0.07 and 0.1. Our models are also designed to reproduce the bright-end galaxy luminosity functions (LFs) in deep *HST*/WFC3 surveys at $z > 6$ involving the Lyman-dropout galaxy samples. This normalization at the bright end of galaxy luminosities puts strong constraints on the intensity.

This paper is organized as follows. In Section 2, we outline our model for the reionization galaxies including stellar nebulae and the IGM emission. Section 3 presents the calculation related to luminosity mass density of these galaxies. In Sections 4– 6, we outline the background intensity and spatial anisotropy power spectrum calculations, respectively. In Section 7, we discuss our results related to the intensity and angular power spectrum and present a comparison to existing measurements. We conclude with a summary in Section 8. We assume the flat ΛCDM model with $\Omega_{\rm m} = 0.27, \Omega_{\rm b} = 0.046, \Omega_\Lambda = 0.73, h = 0.71, \sigma_8 = 0.81$, and $n_{\rm s} = 0.96$ (Komatsu et al. 2011) throughout the paper.

2. EMISSION FROM STARS AND THE INTERGALACTIC MEDIUM

We first describe the emission from stars in first-light galaxies present during reionization. Following Fernandez & Komatsu (2006), we consider two stellar populations in this calculation. The first, referred to as Pop II stars, are metal-poor stars with metallicity $Z = 1/50\, Z_\odot$, and the second, Pop III stars, are metal-free stars with $Z = 0$.

To describe the stellar initial mass function (IMF), we make use of two descriptions. For Pop II stars, we adopt the IMF given by Salpeter (1955)

$$f(M_*) \propto M_*^{-2.35}, \tag{1}$$

with mass range from 3 to 150 $M_\odot$. For Pop III stars, we use the IMF obtained by Larson (1998), which takes the form as

$$f(M_*) = M_*^{-1} \left(1 + \frac{M_*}{M_*^c}\right)^{-1.35}, \tag{2}$$

where $M_*^c = 250\, M_\odot$, and the mass range is from 3 to 500 $M_\odot$.

We utilize the fitting results from Lejeune & Schaerer (2001) and Schaerer (2002) to calculate other stellar parameters, such as the intrinsic bolometric luminosity $L_*^{\rm bol}(M_*)$, the effective temperature $T_*^{\rm eff}(M_*)$, the main-sequence lifetime τ_*, and the time-averaged hydrogen photoionization rate $\overline{Q}_{\rm H\,I}(M_*)$. The fitting forms of these parameters are different for Pop II and Pop III stars. For Pop II stars, they are given as

$$\begin{aligned}
\log_{10}(L_*^{\rm bol}/L_\odot) &= 0.138 + 4.28x - 0.653x^2,\\
\log_{10}(T_*^{\rm eff}/{\rm K}) &= 3.92 + 0.704x - 0.138x^2,\\
\log_{10}(\tau_*/{\rm yr}) &= 9.59 - 2.79x + 0.63x^2,\\
\log_{10}(\overline{Q}_{\rm H\,I}/{\rm s}^{-1}) &= 27.80 + 30.68x - 14.80x^2 + 2.50x^3,
\end{aligned}$$

where $x = \log_{10}(M_*/M_\odot)$ and for Pop III stars, they are

$$\begin{aligned}
\log_{10}(L_*^{\rm bol}/L_\odot) &= 0.4568 + 3.897x - 0.5297x^2,\\
\log_{10}(T_*^{\rm eff}/{\rm K}) &= 3.639 + 1.501x - 0.5561x^2 + 0.07005x^3,\\
\log_{10}(\tau_*/{\rm yr}) &= 9.785 - 3.759x + 1.413x^2 - 0.186x^3,
\end{aligned}$$

[3] http://zebra.caltech.edu

$$\log_{10}(\overline{Q}_{\rm H\,I}/{\rm s}^{-1}) = \begin{cases} 39.29 + 8.55x & 5\text{–}9\ M_\odot \\ 43.61 + 4.90x - 0.83x^2 & 9\text{–}500\ M_\odot \end{cases}.$$

From these expressions, the stellar radius $R_*(M_*)$ is

$$4\pi R_*^2(M_*) = \frac{L_*^{\rm bol}(M_*)}{\sigma T_*^{\rm eff}(M_*)^4}, \quad (3)$$

where $\sigma = 5.67 \times 10^{-5}$ erg s^{-1} cm^{-2} K^{-4} is the Stefan–Boltzmann constant. The stellar radius is useful for the calculation related to the stellar emission spectrum (see Section 3.1).

The ionization volume in the nebulae surrounding the stars (Strömgren sphere) can be derived if assuming ionization equilibrium where the ionization rate equals recombination rate

$$V_{\rm ion}^{\rm neb} = \frac{\overline{Q}_{\rm H\,I}(M_*)}{n_e^{\rm neb} n_{\rm H\,II}^{\rm neb} \alpha_{\rm B}^{\rm rec}}, \quad (4)$$

where $\alpha_{\rm B}^{\rm rec}$ is the hydrogen case B recombination coefficient, which depends on the gas temperature $T_{\rm gas}$ (assumed to be $\simeq 3 \times 10^4$ K); we will discuss this in detail in the next section. Here, $n_e^{\rm neb}$ and $n_{\rm H\,II}^{\rm neb}$ are the local number density of electron and H II in the stellar nebulae where we assume $n_e^{\rm neb} = n_{\rm H\,II}^{\rm neb} = 10^4$ cm^{-3}.

For the IGM, the hydrogen density is lower than that of the stellar nebulae, so we no longer assume the ionization equilibrium. We estimate the ionization volume by a redshift-dependent form as (Santos et al. 2002)

$$V_{\rm ion}^{\rm IGM}(z) = \frac{\overline{Q}_{\rm H\,I}(M_*)}{\bar{n}_{\rm H}(z)} \tau_*, \quad (5)$$

where $\bar{n}_{\rm H}(z) = 1.905 \times 10^{-7}(1+z)^3$ cm^{-3} is the mean hydrogen number density for $\Omega_b = 0.046$ assumed in this work (Shull et al. 2011).

These quantities discussed here would now be used to estimate the luminosity mass density, near-IR background intensity SED, and the anisotropy power spectrum. We make use of emission from the stellar nebulae and the IGM for both Pop II and Pop III stars in galaxies present during reionization.

3. LUMINOSITY MASS DENSITY OF THE SOURCES

In this section, we calculate the luminosity per stellar mass at frequency ν, i.e., luminosity mass density, for several sources that contribute to the infrared background, such as the direct emission from the stars, Lyα line, and free–free, free–bound, and two-photon processes. The luminosity mass density takes the central role in our estimation of the near-IR background intensity spectrum.

3.1. Stellar Spectrum

For simplicity, we assume the stellar spectrum is a Planckian truncated at $h\nu = 13.6$ eV. Thus, the stellar luminosity at frequency ν can be expressed as

$$L_\nu^* = \begin{cases} \pi S_* B_\nu(T_*^{\rm eff}) & \text{for } h\nu < 13.6 \text{ eV} \\ 0 & \text{for } h\nu \geqslant 13.6 \text{ eV} \end{cases},$$

where $S_* = 4\pi R_*^2$ is the surface area of the star, R_* is the stellar radius, M_* is the stellar mass, and $B_\nu(T)$ is the Planck spectrum

$$B_\nu(T_*^{\rm eff}) = \frac{2h\nu^3/c^2}{e^{h\nu/kT} - 1}. \quad (6)$$

Note that for simplicity we have ignored the absorption lines of the Lyα series here. The absorption is not strong enough to affect the shape of the spectrum and hence it is not expected to affect our results especially in the infrared wavelengths (Santos et al. 2002; Fernandez & Komatsu 2006). Our predictions related to the optical background fluctuations may be somewhat overestimated. Also, the emission with $h\nu \geqslant 13.6$ eV cannot be approximated by a blackbody spectrum, thus we use the fitting formulae for time-averaged photoionization rate, $\overline{Q}_{\rm H\,I}$, for Pop II and Pop III stars to calculate the emission at higher energies.

3.2. Lyα Emission

The luminosity of Lyα emission at a frequency ν is

$$L_\nu^{{\rm Ly}\alpha} = h\nu_{{\rm Ly}\alpha}\left(\epsilon_{{\rm Ly}\alpha}^{\rm rec} + \epsilon_{{\rm Ly}\alpha}^{\rm coll}\right)\phi(\nu_{{\rm Ly}\alpha} - \nu, z)V(M_*), \quad (7)$$

where $\nu_{{\rm Ly}\alpha}$ is the frequency of Lyα photons, and $V(M_*)$ is the emission volume that can be estimated by Equations (4) and (5) for the stellar nebulae and the IGM, respectively. Here, $\epsilon_{{\rm Ly}\alpha}^{\rm rec}$ is the Lyα recombination emission rate per cm^3, which is given by

$$\epsilon_{{\rm Ly}\alpha}^{\rm rec} = f_{{\rm Ly}\alpha}^{\rm rec} n_e n_{\rm H\,II} \alpha_{\rm B}^{\rm rec},$$

where n_e is the electron number density, $n_{\rm H\,II}$ is the H II number density, $\alpha_{\rm B}^{\rm rec}$ is the hydrogen case B recombination coefficient, and $f_{{\rm Ly}\alpha}^{\rm rec}$ is the fraction of the Lyα photons produced in the case B recombination. This fraction can be estimated through the fitting formula (Cantalupo et al. 2008)

$$f_{{\rm Ly}\alpha}^{\rm rec}(T) = 0.686\text{–}0.106\log_{10}(T_4) - 0.009T_4^{-0.44}, \quad (8)$$

where $T_4 = T/10^4$ K, which is accurate to 0.1% for 100 K $< T < 10^5$ K. Note that this fraction is actually not sensitive to the temperature, so it can be treated as a constant $\sim$0.68 in the most cases. The hydrogen case B recombination coefficient $\alpha_{\rm B}^{\rm rec}$ we use here is from Hummer (1994), which is fitted by Seager et al. (1999) as

$$\alpha_{\rm B}^{\rm rec}(T) = 10^{-13}\frac{aT_4^b}{1 + cT_4^d}\ ({\rm cm}^3\ {\rm s}^{-1}), \quad (9)$$

where $a = 4.309$, $b = -0.6166$, $c = 0.6703$, and $d = 0.5300$. We assume a gas temperature of $T_{\rm gas} = 3 \times 10^4$ K in our calculation to obtain $\alpha_{\rm B}^{\rm rec}$.

The $\epsilon_{{\rm Ly}\alpha}^{\rm coll}$ is the collisional emission rate per cm^3 given by

$$\epsilon_{{\rm Ly}\alpha}^{\rm coll} = C_{{\rm Ly}\alpha}^{\rm eff} n_e n_{\rm H\,I}, \quad (10)$$

where $n_{\rm H\,I}$ is the neutral hydrogen number density and $C_{{\rm Ly}\alpha}^{\rm eff}$ is the effective collisional excitation coefficient. It has the form (Cantalupo et al. 2008)

$$C_{{\rm Ly}\alpha}^{\rm eff} = C_{1,2p} + C_{1,3s} + C_{1,3d}\,. \quad (11)$$

Here, we take into account the excitation up to energy level $n = 3$ to produce Lyα photons. The higher level emission can be neglected given the high temperature we consider for this calculation. The excitation collisional rate $C_{l,u}$, in cm^3 per second, can be written as

$$C_{l,u} = \frac{8.629 \times 10^{-6}}{g_l\sqrt{T}}\gamma_{l,u}e^{-E_{l,u}/kT}\ ({\rm cm}^3\ {\rm s}^{-1}), \quad (12)$$

where $E_{l,u}$ is the energy difference between lower level l and higher level u, g_l is the statistic weight for level l, and $\gamma_{l,u}(T)$ is the effective collision strength calculated using the fitting formulae from Giovanardi et al. (1987).

The $\phi(\nu_{\rm Ly\alpha} - \nu, z)$ is the Lyα line profile, and we use the result from Santos et al. (2002) where they fitted the simulated Lyα line profile of Loeb & Rybicki (1999) for a homogeneous and expanding IGM:

$$\phi(\nu_{\rm Ly\alpha} - \nu, z) = \begin{cases} \nu_*(z) d\nu^{-2} \exp[-\nu_*(z)/d\nu] & \text{if } d\nu > 0 \\ 0 & \text{if } d\nu \leqslant 0 \end{cases},$$

where $d\nu = \nu_{\rm Ly\alpha} - \nu$, and

$$\nu_*(z) = 1.5 \times 10^{11}\ {\rm Hz} \left(\frac{\Omega_{\rm b} h^2}{0.019}\right)\left(\frac{h}{0.7}\right)^{-1} \frac{(1+z)^3}{E(z)}.$$

Here $E(z) = H(z)/H_0$, and we assume the flat ΛCDM model and take $E(z) = \sqrt{\Omega_{\rm m}(1+z)^3 + \Omega_\Lambda}$.

3.3. Free–Free and Free–Bound Emission

For free–free and free–bound emission, we again follow the same approach as Fernandez & Komatsu (2006). Following their derivation, the continuum luminosity of these two processes at frequency ν has the same form, with

$$L_\nu^{\rm ff,fb} = 4\pi j_\nu^{\rm ff,fb} V(M_*), \tag{13}$$

where $j_\nu^{\rm ff,fb}$ is the specific emission coefficient for free–free and free–bound emission (Dopita & Sutherland 2002)

$$j_\nu^{\rm ff,fb} = 5.44 \times 10^{-39} \frac{e^{-h\nu/kT}}{\sqrt{T}} n_e n_p g_{\rm eff}^{\rm ff,fb} \times ({\rm erg\,cm^{-3}\,s^{-1}\,Hz^{-1}\,sr^{-1}}). \tag{14}$$

Here, n_p is the proton number density, T is the gas temperature, and $g_{\rm eff}^{\rm ff,fb}$ is effective Gaunt factor for free–free and free–bound emission, which takes the form as

$$g_{\rm eff}^{\rm ff,fb} = \begin{cases} \bar{g}_{\rm ff} & \text{free–free} \\ \frac{x_n e^{x_n}}{n} g_{\rm fb}(n) & \text{free–bound} \end{cases}, \tag{15}$$

where $\bar{g}_{\rm ff} \simeq 1.1$ is the thermal averaged Gaunt factor of free–free emission and $g_{\rm fb}(n) \simeq 1.05$ is the free–bound emission Gaunt factor for a different energy level n. These values have an accuracy of 10% (Larzas & Latter 1961). In Equation (15) $x_n = R_y/(kT_g n^2)$, where Ry/kT_g is around 10 for the parameter space we are interested in (Fernandez & Komatsu 2006). The energy level n is determined by the emission photon frequency ν. If $cR_y/n'^2 < \nu < cR_y/(n'-1)^2$, and then $n = n'$ where $R_y = 1.1 \times 10^7\ {\rm m^{-1}}$ is the Rydberg constant. Note that the n here starts at $n = 2$, since the photons from $n = 1$ can be easily absorbed by other neutral hydrogen atoms and be ionized instantly.

3.4. Two-photon Emission

For the two-photon process, we also follow the approach of Fernandez & Komatsu (2006) and write the luminosity as

$$L_\nu^{\rm 2ph} = \frac{2h\nu}{\nu_{\rm Ly\alpha}} P(\nu/\nu_{\rm Ly\alpha}) \epsilon_{\rm 2ph} V(M_*), \tag{16}$$

where $\epsilon_{\rm 2ph} = f_{\rm 2ph} n_e n_{\rm H\,II} \alpha_{\rm B}^{\rm rec}$ is the two-photon emission rate per cm^3, and $f_{\rm 2ph} \simeq (1 - f_{\rm Ly\alpha}^{\rm rec})$. The $P(\nu/\nu_{\rm Ly\alpha})d\nu/\nu_{\rm Ly\alpha}$ is the normalized probability of generating one photon in the range $d\nu/\nu_{\rm Ly\alpha}$ from per two-photon decay. We use the fitting formula derived in Fernandez & Komatsu (2006)

$$P(y) = 1.307 - 2.627(y-0.5)^2 + 2.563(y-0.5)^4 - 51.69(y-0.5)^6,$$

where $y = d\nu/\nu_{\rm Ly\alpha}$, which is a good fit to the data given in Brown & Mathews (1970).

3.5. Luminosity Mass Density and Total Emission

Then following Fernandez & Komatsu (2006) and Fernandez et al. (2010), we can derive the mean luminosity mass density for each emission source by integrating over the IMF for the Pop II or Pop III stars

$$l_\nu = \frac{\int dM_* f(M_*) L_\nu(M_*)}{\langle M_* \rangle}, \tag{17}$$

where the ranges of the integral are from 3 to 150 $M_\odot$ with the IMF given by Salpeter (1955) for Pop II stars, and from 3 to 500 $M_\odot$ with the IMF in Larson (1998) for Pop III stars. Here, the average mass $\langle M_* \rangle$ is given as

$$\langle M_* \rangle = \int_0^\infty dM_*\ M_* f(M_*)\,, \tag{18}$$

where $f(M_*)$ is the normalized IMF with

$$\int_0^\infty dM_* f(M_*) = 1.$$

Note that this expression is only valid when the main-sequence lifetime is larger than the star formation timescale. Otherwise, it should be evaluated by

$$l_\nu = \frac{\int dM_* f(M_*) L_\nu(M_*) \tau_*(M_*)}{t_{\rm SF}(z) \langle M_* \rangle}. \tag{19}$$

Here, $t_{\rm SF}$ is the star formation timescale, which is given by

$$t_{\rm SF}(z) = \left(\frac{d\ln\rho_*(z)}{dt}\right)^{-1}, \tag{20}$$

where $\rho(z)$ is the stellar mass density at z, which is related with the comoving star formation rate density (SFRD) as $\psi(z) = d\rho_*(z)/dt$. We use the halo mass function to calculate $\psi(z)$ and $\rho_*(z)$ and the details are described in the next section. We note that the $t_{\rm SF}$ is important for the estimation of the l_ν as discussed in Fernandez et al. (2010).

Finally, we obtain the total luminosity mass density from the stellar nebulae

$$l_\nu^{\rm neb} = l_\nu^* + (1 - f_{\rm esc})(l_\nu^{\rm Ly\alpha} + l_\nu^{\rm ff} + l_\nu^{\rm fb} + l_\nu^{\rm 2ph}) \tag{21}$$

and the same from the IGM

$$l_\nu^{\rm IGM} = f_{\rm esc}(l_\nu^{\rm Ly\alpha} + l_\nu^{\rm ff} + l_\nu^{\rm fb} + l_\nu^{\rm 2ph}), \tag{22}$$

where $f_{\rm esc}$ is the escape fraction of the ionization photons that propagate into the IGM from the nebulae surrounding the stars.

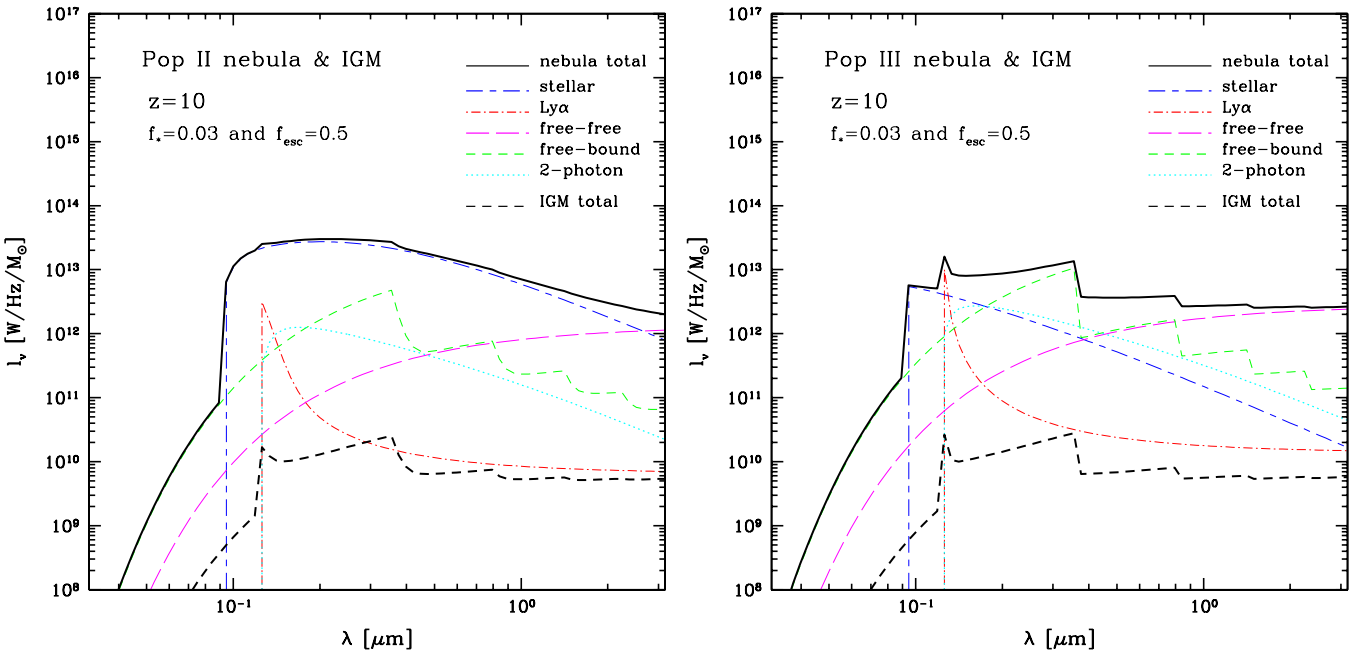

Figure 1. Luminosity mass density l_ν vs. the rest-frame wavelength λ for the Pop II and Pop III stars at $z = 10$. The total l_ν from the stellar nebula and the IGM are shown in both panels (thick lines). Also, to specify the contribution from different sources, we plot the l_ν of stellar, Lyα, free–free, free–bound, and two-photon emission for the stellar nebula case (thin lines). We take $f_* = 0.03$ and $f_{\rm esc} = 0.5$ for both Pop II and Pop III cases. We find the l_ν of the stellar nebula is much larger than that of the IGM for both Pop II and Pop III stars.

(A color version of this figure is available in the online journal.)

In Figure 1, we show the total luminosity mass density as a function of the rest-frame wavelength λ from the stellar nebula and the IGM for Pop II and Pop III stars, respectively. The contributions from the different sources we consider are also shown for the stellar nebula case. Here, we set $f_* = 0.03$ and $f_{\rm esc} = 0.5$ for both Pop II and Pop III cases.

With these parameters we find that the stellar spectrum is dominant for Pop II stars while the "background" spectrum, such as Lyα and free–bound, is comparable with or even larger than the stellar spectrum for Pop III stars. Also, as can be seen, the l_ν from the IGM is much lower than that from the stellar nebula for both Pop II and Pop III cases, and the total l_ν from the Pop III stars is similar to that from the Pop II stars. These results are already discussed in Fernandez & Komatsu (2006).

4. REIONIZATION HISTORY AND UV LUMINOSITY DENSITY

To test if the reionization history associated with our stellar model is consistent with that of the current observations, such as *WMAP* seven-year results (Komatsu et al. 2011), we need to calculate the hydrogen reionization fraction $x_{\rm H\,II}(z)$ as a function of redshift. Following Madau et al. (1998), $x_{\rm H\,II}(z)$ can be estimated as

$$\frac{dx_{\rm H\,II}}{dt} = \frac{f_{\rm esc}\psi(z)q(z)}{\bar{n}_{\rm H}(z)} - \frac{x_{\rm H\,II}}{\bar{t}_{\rm rec}}, \qquad (23)$$

where $z_{\rm i}$ is the redshift of the beginning of the reionization epoch (we take $z_{\rm i} = 30$), $\psi(z)$ is the comoving SFRD, and the function $q(z)$ is defined as $q(z) \equiv (\overline{Q}_{\rm H\,I}/\langle M_*\rangle)\langle\tau_*\rangle$. Here, $\langle\tau_*\rangle$ is the average stellar lifetime which is given by $\langle\tau_*\rangle = \int_0^\infty dM_*\, \tau_*(M_*) f(M_*)$, and $t_{\rm rec}$ is the volume averaged recombination time, which can be written as

$$\bar{t}_{\rm rec} = \left[C_{\rm H\,II}(z)\alpha_{\rm B}^{\rm rec}\bar{n}_{\rm H}(z)(1 + Y/4X)\right]^{-1}, \qquad (24)$$

where $C_{\rm H\,II} \equiv \langle n_{\rm H\,II}^2\rangle/\langle n_{\rm H\,II}\rangle^2$ is the clumping factor of ionized hydrogen. Here we adopt the simulation result from Trac & Cen (2007). $X = 0.75$ and $Y = 0.25$ are the mass fractions of hydrogen and helium, respectively. Note that we have already considered the escape fraction $f_{\rm esc}$, so the $C_{\rm H\,II}$ here is the clumping factor excluding the halos with star formation.

For the comoving SFRD we consider the ongoing star formation model (Santos et al. 2002):

$$\psi(z) = f_* \frac{\Omega_{\rm b}}{\Omega_{\rm m}} \frac{d}{dt} \int_{M_{\rm min}}^\infty dM\, M \frac{dn}{dM}(M, z), \qquad (25)$$

where f_* is the star formation efficiency which denotes the fraction of baryons converted to stars, dn/dM is the halo mass function (Sheth & Tormen 1999), and $M_{\rm min}$ is the threshold mass for a dark matter halo to form a galaxy during reionization. This minimum mass is taken to be a free parameter and is varied to fit a combination of the *WMAP* seven-year optical depth and the galaxy LF, as we discuss in Section 6.

We also need a stellar population evolution model to describe $q(z)$ with the relative fraction of the Pop II and Pop III stars at different redshifts. In principle, there should be a cutoff at some redshift for Pop III stars as they are not expected to form at low redshifts once the gas is polluted by metals. We assume this cutoff is not lower than $z = 6$ when the universe is fully ionized. We use the error function to denote the population fraction as

$$f_{\rm P}(z) = \frac{1}{2}\left[1 + {\rm erf}\left(\frac{z_{\rm t} - 10}{\sigma_{\rm P}}\right)\right], \qquad (26)$$

where $\sigma_{\rm P} = 0.5$ is the population transition width. Then, the term $q(z)$ in Equation (23) can be expressed by

$$q(z) = f_{\rm P}\frac{\overline{Q}_{\rm H\,I}^{\rm PopIII}}{\langle M_*^{\rm PopIII}\rangle}\langle\tau_*^{\rm PopIII}\rangle + (1 - f_{\rm P})\frac{\overline{Q}_{\rm H\,I}^{\rm PopII}}{\langle M_*^{\rm PopII}\rangle}\langle\tau_*^{\rm PopII}\rangle. \qquad (27)$$

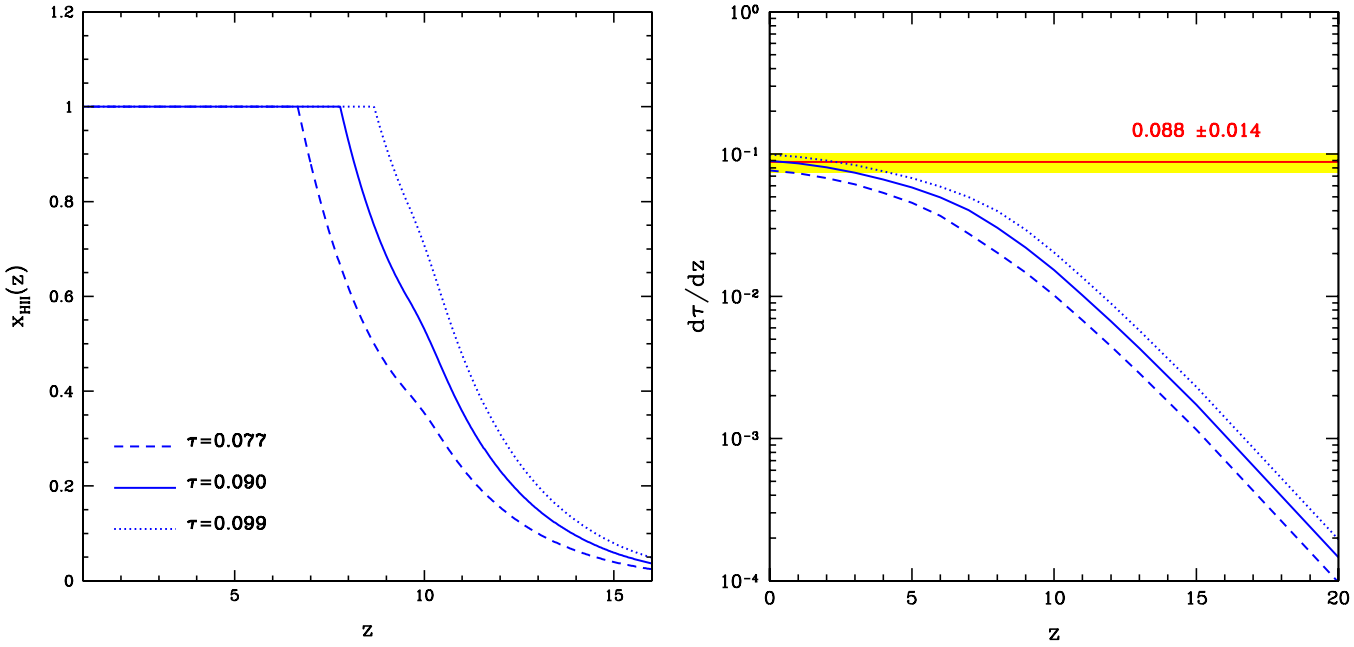

Figure 2. Left: the hydrogen reionization fraction $x_{\rm H\,II}$ as a function of redshift z for three cases of the $f_* = 0.02$, 0.03, and 0.04. The solid line with $f_* = 0.03$ indicates the optical depth $\tau = 0.090$, which is close to the result of *WMAP* seven-year, which gives $\tau = 0.088 \pm 0.014$. The dashed and dotted lines are derived with $f_* = 0.02$ and 0.04, which denote $\tau = 0.077$ and 0.099, respectively. Right: the dependence of the optical depth on the minimum redshift in Equation (28). The blue solid, dashed, and dotted lines are for the three stellar models with $f_* = 0.03$, 0.02, and 0.04, respectively. The result of *WMAP* seven-year is also shown in red solid line with yellow 1σ error region for comparison.

(A color version of this figure is available in the online journal.)

As our default model, we assume that the Pop III stars are mainly dominant for $z \gtrsim 10$ while Pop II stars are for $z \lesssim 10$ with $z_{\rm t} = 10$. When we present our results we also show results for three additional values of the transition from $z_{\rm t} = 10$ to 30.

We estimate the optical depth to electron scattering with the reionization fraction $x_e(z)$ as

$$\tau = \int_0^\infty dz \frac{c}{H(z)} \frac{n_e(z)\sigma_{\rm T}}{1+z}, \tag{28}$$

where $\sigma_{\rm T} = 6.65 \times 10^{-29}$ m^2 is the Thompson scattering cross-section, and $n_e(z) = x_{\rm H\,II}(z)\bar{n}_{\rm H}(z)(1 + \eta Y/4X)$ is the electron number density of the universe at redshift z, and we assume the helium is singly ionized for $z > 4$ ($\eta = 1$) and doubly ionized for $z < 4$ ($\eta = 2$) (Kuhlen & Faucher-Giguere 2012).

In Figure 2, we plot the hydrogen reionization fraction $x_{\rm H\,II}$ versus z for three optical depth τ with three stellar models. The blue solid line denotes the $\tau = 0.090$ with $f_* = 0.03$, which is close to the result of *WMAP* seven-year data with $\tau = 0.088 \pm 0.014$ (Komatsu et al. 2011). In this case, reionization ends around $z_{\rm e} \simeq 8$, which is consistent with the current studies, and we find that Pop III stars can ionize the universe to ~60% by $z = 10$ and Pop II stars are responsible for the rest of the reionization over an interval $\Delta z \simeq 2$.

For $f_* = 0.02$ and 0.04, we find $\tau = 0.077$ (shown with a dashed line) and $\tau = 0.099$ (shown with a dotted line), respectively. These two reionization histories are such that $z_{\rm e} \sim 6.5$ and 9, respectively. For case with $\tau = 0.077$, the Pop III stars ionize ~40% of the universe and the Pop II stars are needed over the interval $\Delta z \simeq 3.5$ to complete reionization. For the third case with $\tau = 0.099$, Pop III stars ionize 80% of the universe at $z = 10$ with Pop II stars completing the rest 20% in an interval of $\Delta z \simeq 1$

In Figure 2, we also show the dependence of the optical depth on the minimum redshift $z_{\rm min}$ in Equation (28). The blue solid, dashed, and dotted lines are for the three stellar models with $\tau = 0.090$, 0.077, and 0.099, respectively, for $z_{\rm min} = 0$. The *WMAP* seven-year result with $\tau = 0.088 \pm 0.014$ is also shown with a red solid line and a yellow 1σ error region. We find that the slope of the curves is steeper for $z_{\rm min} > 10$ and flatter for $z_{\rm min} < 10$, which is caused by the Pop III to Pop II transition around $z = 10$ in our model. Note that this transition is arbitrarily chosen. We varied the transition redshift and also cases where Pop II and Pop III stars are mixed in with different fractions at different redshifts. In all these cases, we found results that are generally consistent with each other. Thus, the three choices related to the reionization history that we show here to keep this presentation simple are not biased with respect to the final result related to the IR background intensity that we are trying to estimate in this paper.

We also estimate the total number of ionizing photons per baryon required to maintain the ionized IGM between $z_{\rm end}$ and z,

$$N^p_{\rm ion}(z) = N_{\rm end} + \int_z^{z_{\rm end}} \frac{x_{\rm H\,II}(z')}{t_{\rm rec}} \frac{dt}{dz'} dz', \tag{29}$$

where $z_{\rm end} = 6$ is the redshift of the end of the reionization, and if we assume the helium is also totally singly ionized at $z_{\rm end} = 6$ we can get $N_{\rm end} \simeq 1$. In Figure 3, we show the $N^p_{\rm ion}(z)$ at different z for three f_* cases. We find the number keeps going up until around $z = 15$ and becomes constant ~2.5 at higher redshift for three cases of the reionization histories.

5. THE NEAR-IR EBL INTENSITY FROM REIONIZATION

The mean cosmic infrared background can be estimated by

$$\nu_{\rm obs} \bar{I}_{\nu_{\rm obs}} = \int_{z_{\rm min}}^{z_{\rm max}} dz \frac{c}{H(z)} \frac{\nu(z)\bar{j}_\nu(z)}{(1+z)^2}, \tag{30}$$

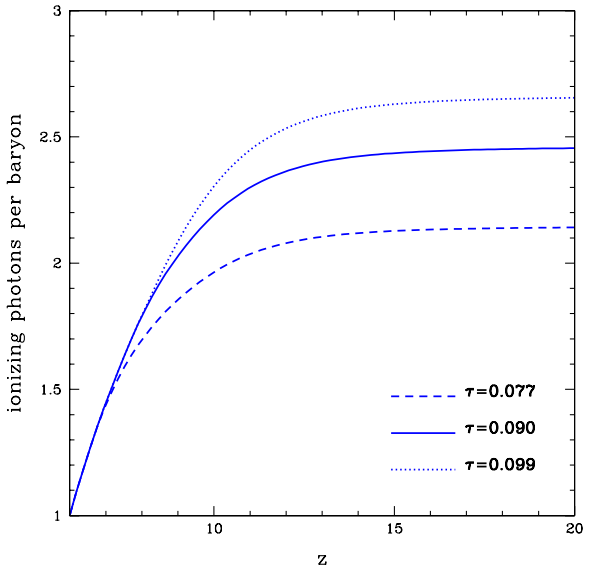

Figure 3. Total number of ionizing photons per baryon to maintain the ionized IGM between the redshift of the end of the reionization and z. The blue dotted, solid, and dashed lines are derived from the model with $f_* = 0.02$, 0.03, and 0.04, respectively.

(A color version of this figure is available in the online journal.)

where $\nu(z) = (1+z)\nu_{\rm obs}$, and we take $z_{\rm min} = 6$ and $z_{\rm max} = 30$ in the calculation. This redshift range can fully take account of the emission from the Pop III and early Pop II stars, which is redshifted into the near-IR band. We take this to be the form of

$$\bar{j}_\nu(z) = f_{\rm P}\bar{j}_\nu^{\rm PopIII}(z) + (1-f_{\rm P})\bar{j}_\nu^{\rm PopII}(z), \quad (31)$$

where $\bar{j}_\nu^{\rm PopIII}$ and $\bar{j}_\nu^{\rm PopII}$ are the comoving specific emission coefficients

$$\bar{j}_\nu^i(z) = \frac{1}{4\pi} l_\nu^i \langle \tau_*^i \rangle \psi(z), \quad (32)$$

where l_ν^i is the luminosity mass density at ν, $\langle \tau_*^i \rangle$ is the mean stellar lifetime of each of the stellar type, and $\psi(z)$ is the comoving SFRD given by Equation (25).

In Figure 4, we show the spectrum I_ν of the near-IR background light intensity from both Pop II and Pop III stars. We assume that the reionization is ending around $z = 6$ and integrate up to $z = 30$ to determine I_ν. Similar to Figure 1, we plot the total spectrum from the stellar nebula and the IGM for both Pop II and Pop III stars. The contributions from different sources we consider are also shown as colored thin lines.

Here, we still take the same value for f_* and $f_{\rm esc}$ as in Figure 1 related to the l_ν calculation. Similar to the luminosity mass density, the spectrum from stellar nebula is much larger than that from the IGM, and the stellar spectrum is higher for Pop II stars while the "background" spectrum is higher for Pop III stars. However, unlike the case of the luminosity mass density, we now find the spectrum from Pop II stars is larger than that from Pop III stars. This is basically because the typical lifetime of Pop II stars is longer than that of the Pop III stars.

6. ANGULAR POWER SPECTRUM

The angular cross power spectrum of the infrared emission at observed frequencies ν and ν' for a multipole ℓ is

$$C_\ell^{\nu\nu'} = \int_{z_{\rm min}}^{z_{\rm max}} dz \left(\frac{d\chi}{dz}\right)\left(\frac{a}{\chi}\right)^2 \bar{j}_\nu(z)\bar{j}_{\nu'}(z) P_{\rm gg}(k,z), \quad (33)$$

where χ is the comoving angular diameter distance, $a = (1+z)^{-1}$ is the scale factor, and $\bar{j}_\nu(z)$ is the mean emission per comoving volume at frequency ν and redshift z. If we just take account of the flux lower than an upper cutoff $S_{\rm cut}$, then $\bar{j}_\nu(z)$ can be written as

$$\bar{j}_\nu(z) = (1+z)\int_0^{S_{\rm cut}} dS\, S \frac{d^2N}{dSdz}. \quad (34)$$

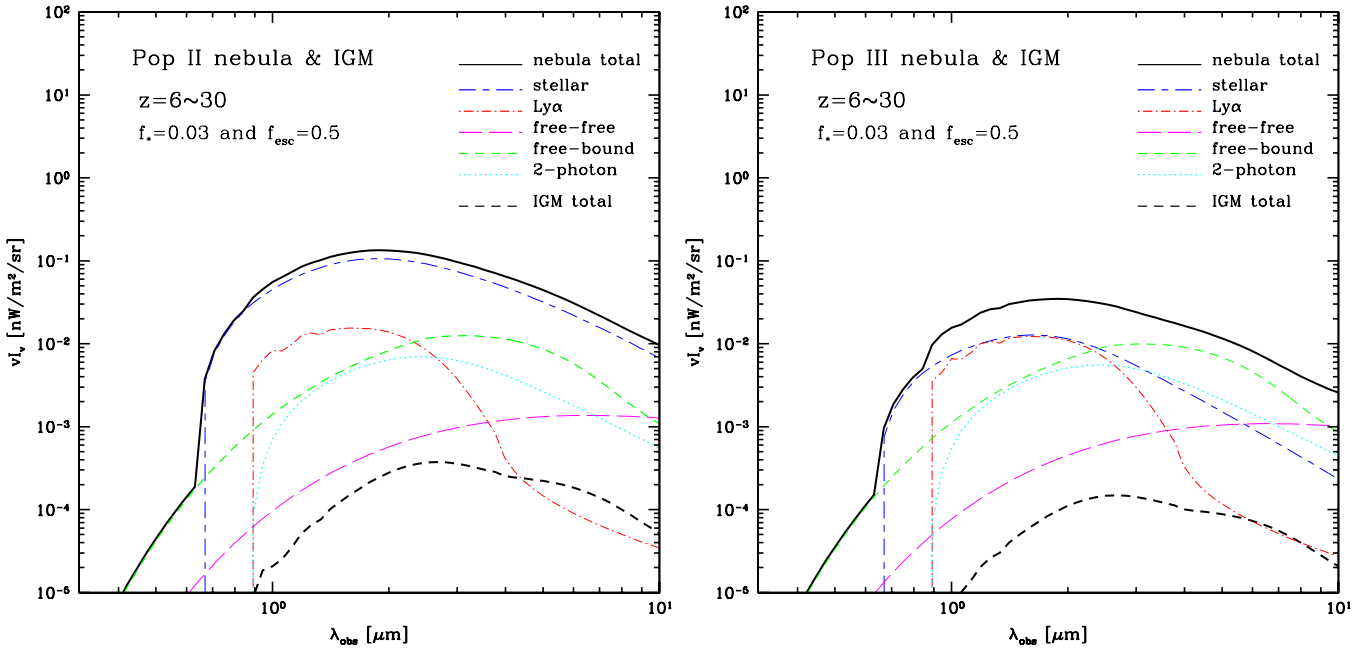

Figure 4. Spectrum of the near-IR EBL intensity vs. the observed frame wavelength $\lambda_{\rm obs}$ for the Pop II and Pop III stars integrated from $z = 6$ to 30. We take $f_* = 0.03$ and $f_{\rm esc} = 0.5$ for both Pop II and Pop III cases. We find the spectrum of the stellar nebula is much larger than that from the IGM for both Pop II and Pop III stars, which is similar to what is shown in Figure 1. However, unlike the luminosity density case, the spectrum from the Pop II stars, is larger than that from the Pop III stars. This is basically because the typical lifetime of the Pop II stars is longer than that of Pop III stars.

(A color version of this figure is available in the online journal.)

Here, S is the source flux and N is the number of sources. This quantity is just the comoving specific emission coefficient that we derived in the last section. The $P_{gg}(k, z)$ is the galaxy power spectrum at wavenumber $k = \ell/\chi$ and redshift z, and we will make use of the model of halo occupation distribution (HOD) to calculate the $P_{gg}(k, z)$.

6.1. First Galaxy Clustering

To calculate the P_{gg}, we extend the linear theory model of Cooray et al. (2004) and make use of the HOD for first-light galaxies during reionization. The galaxy power spectrum can be written as

$$P_{gg}(k, z) = P_{gg}^{1h}(k, z) + P_{gg}^{2h}(k, z), \tag{35}$$

where P_{gg}^{1h} and P_{gg}^{2h} denote the power spectrum contributed by galaxies in a single dark matter halo and galaxies in two different dark matter halos, respectively. Then we can write (Cooray & Sheth 2002)

$$P_{gg}^{1h} = \int dM \, \frac{dn}{dM} \frac{\langle N_{gal}(N_{gal} - 1)\rangle}{\bar{n}_{gal}^2} u^p(M, k), \tag{36}$$

$$P_{gg}^{2h} = P_{lin}\left[\int dM \, b(M, z) \frac{dn}{dM} \frac{\langle N_{gal}\rangle}{\bar{n}_{gal}} u(M, k)\right]^2. \tag{37}$$

Here, M is the halo mass, $dn/dM(M, z)$ is the halo mass function, $u(M,k)$ is the Fourier transform of the Navarro–Frenk–White (NFW) halo density profile (Navarro et al. 1995), $p = 1$ when $\langle N_{gal}(N_{gal} - 1)\rangle \leqslant 1$ and $p = 2$ otherwise (Cooray & Sheth 2002), $b(M,z)$ is the halo bias (Sheth & Tormen 1999), and $P_{lin}(k, z)$ is the linear matter power spectrum (Eisenstein & Hu 1997). $\bar{n}_{gal}$ is the mean number density of galaxies, which is given by

$$\bar{n}_{gal}(z) = \int dM \frac{dn}{dM} \langle N_{gal}\rangle. \tag{38}$$

$\langle N_{gal}\rangle$ is the mean number of galaxies in a halo with mass M, which is the sum of number of central galaxies and satellite galaxies (Zheng et al. 2005)

$$\langle N_{gal}\rangle = \langle N_{cen}\rangle + \langle N_{sat}\rangle, \tag{39}$$

where we define

$$\langle N_{cen}\rangle = \frac{1}{2}\left[1 + \mathrm{erf}\left(\frac{\log M - \log M_{min}}{\sigma_{\log M}}\right)\right], \tag{40}$$

and

$$\langle N_{sat}\rangle = \frac{1}{2}\left[1 + \mathrm{erf}\left(\frac{\log M - \log M_0}{\sigma_{\log M}}\right)\right]\left(\frac{M}{M_{sat}}\right)^{\alpha_s}. \tag{41}$$

In this definition, M_{min} denotes the mass of a halo that has 50% probability of hosting a central galaxy, and $\sigma_{\log M}$ is the transition width. For the satellite galaxies, M_0 is the truncation mass for satellites, M_{sat} is the normalization mass, and α_s denotes the slope of the power-law relation about the halo mass M. We assume M_0 is always larger than M_{min}, since there should not be satellites without central galaxy, and assume $M_0 = 2\,M_{min}$. We take $M_{sat} = 15\,M_{min}$, $\sigma_{\log M} = 0.3$, and $\alpha_s = 1.5$ in this paper. If assuming a Poisson distribution for satellite galaxies, we can obtain

$$\langle N_{gal}(N_{gal} - 1)\rangle \simeq 2\langle N_{sat}\rangle\langle N_{cen}\rangle + \langle N_{sat}\rangle^2. \tag{42}$$

This expression could take account of the case $0 < \langle N_{cen}\rangle < 1$ and is consistent with our definitions for the $\langle N_{cen}\rangle$ and $\langle N_{sat}\rangle$.

6.2. Poisson Fluctuations

The clustering measurements are affected by the Poisson fluctuations associated with the shot noise caused by the discrete and finite number of galaxies from which clustering is measured. Assuming a Poisson distribution the ℓ-independent shot-noise power spectrum is

$$C_\ell^{shot} = \int_0^{S_{cut}} dS \, S^2 \frac{dN}{dS}. \tag{43}$$

To estimate C_ℓ^{shot}, we first define the luminosity mass density for the mass of the dark matter halos at frequency ν

$$l_\nu^h = \frac{L_\nu}{M} \simeq f_* \frac{\Omega_b}{\Omega_m} l_\nu^s,$$

where $l_\nu^s = L_\nu/M_*$ is the luminosity mass density for the stellar mass discussed in Section 3. We derive the three-dimensional shot-noise power spectrum by assuming L_ν is proportional to the halo mass M, i.e., l_ν^h is independent on M

$$P_\nu^{shot}(z) = \left(\frac{l_\nu^h}{4\pi}\right)^2 \int dM \, M^2 \frac{dn}{dM}(M, z). \tag{44}$$

Then the two-dimensional shot-noise power spectrum can be written as

$$C_\ell^{\nu\nu',shot} = \int_{z_{min}}^{z_{max}} dz \left(\frac{d\chi}{dz}\right)\left(\frac{a}{\chi}\right)^2 P_\nu^{shot}(z). \tag{45}$$

6.3. Band-averaged Intensity Power Spectrum

For a specific near-IR observation with a band frequency from ν_1 to ν_2, we can define a band-averaged luminosity mass density as

$$l = \frac{1}{\Delta\nu} \int_{\nu_1(1+z)}^{\nu_2(1+z)} d\nu \, l_\nu, \tag{46}$$

where $\Delta\nu = \nu_2 - \nu_1$ is the bandwidth. Then we can derive the band-averaged comoving specific emission coefficient $\bar{j}(z)$ using Equation (32) and the three-dimensional shot-noise power spectrum P^{shot} using Equation (44), respectively.

Finally, we find the band-averaged angular cross power spectrum and shot-noise power spectrum are

$$C_\ell = \int_{z_{min}}^{z_{max}} dz \left(\frac{d\chi}{dz}\right)\left(\frac{a^2}{\chi}\right)^2 \bar{j}(z)\bar{j}(z) P_{gg}(k, z), \tag{47}$$

and

$$C_\ell^{shot} = \int_{z_{min}}^{z_{max}} dz \left(\frac{d\chi}{dz}\right)\left(\frac{a^2}{\chi}\right)^2 P^{shot}(z), \tag{48}$$

respectively. Note that here we have a factor a^4 instead of a^2 in $C_\ell^{\nu\nu'}$ and $C_\ell^{\nu\nu',shot}$ and this dependence has been explained in the Appendix of Fernandez et al. (2010).

7. RESULTS AND DISCUSSION

In this section, we first estimate the infrared background intensity and then discuss the angular power spectrum as derived previously. We also compare our estimation with the observational data and discuss the dependence of the result on the parameters in the model.

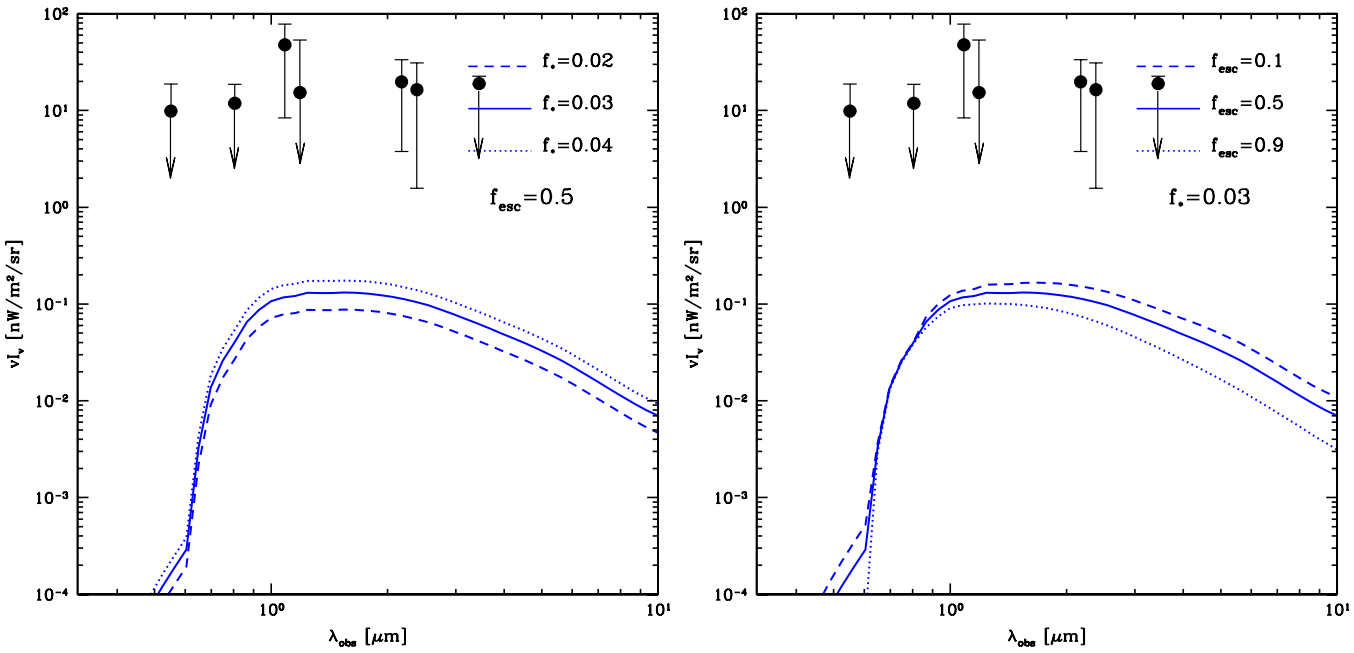

Figure 5. Total near-IR background intensity spectrum for three assumed values of f_* at fixed $f_{\rm esc}$ (left panel) and the same with $f_{\rm esc}$ varied at fixed f_* (right panel). In the left panel, the dashed, solid, and dotted lines denote the three cases of reionization history with $\tau = 0.077$, 0.090, and 0.099, respectively. The models in the right panel also range in τ between 0.07 and 0.1. The data points with error bars are from Santos et al. (2002) and show the "DIRBE excess" defined as the difference between total DIRBE background and the integrated galaxy light at each of the wavelengths. The points shown with arrows are strictly upper limits since the low end of the error is consistent with zero for them with significance less than 2σ.

(A color version of this figure is available in the online journal.)

7.1. Near-IR EBL from Reionization

In Figure 5, we show the spectrum of the near-IR intensity versus the observed frequency for three cases of the reionization history with $\tau = 0.077$, 0.090, and 0.099 corresponding to $f_* = 0.02$, 0.03, and 0.04. Here, the spectrum is the total spectrum of the sum of that from both stellar nebula and the IGM, which are calculated by putting Equation (31) into Equation (30). Also, we set $f_{\rm esc} = 0.5$ for both Pop II and Pop III stars. The right panel of Figure 5 shows three cases with $_{\rm esc}$ varied at fixed f_*. In both panels, for comparison, we plot the observational data in terms of the excess of EBL relative to the IGL of known galaxy populations at low redshifts (Madau & Pozzetti 2000). The excess EBL data plotted here are the same as those shown in Santos et al. (2002) and involve measurements mainly from DIRBE with various models for zodiacal light and Galactic stellar contribution.

We find that the emission from the Pop II stars dominates the spectrum for all of the three cases. As we have just discussed in the last section, this is because the lifetime of the Pop II is longer than the Pop III stars. In the spectrum, the shorter and longer wavelength parts are mainly contributed by the "background" spectrum from Pop III stars while the medium part by Pop II stellar spectrum, so if just the Pop III stars get longer lifetime, only the "background" spectrum can be effectively reinforced in the total spectrum.

In any case, regardless of assumptions related to the stellar type, we find that the EBL intensity from reionization is no more than 0.4 nW m^{-2} sr^{-1}. Such an intensity is significantly smaller than the previous predictions that attempted to explain almost all or a significant fraction of the excess EBL seen in DIRBE data relative to IGL estimates. An intensity larger than about 2.5 nW m^{-2} sr^{-1} in the J band could be in conflict with metal production considerations and the X-ray background (Madau & Silk 2005), though they do not necessarily require high efficiency factors to generate the required star formation (Fernandez & Komatsu 2006). The difference between our calculation and the previous ones is that we primarily require the reionization model to generate a reionization history consistent with the *WMAP* optical depth. This limits the number of H-ionizing photons per baryon during reionization to be less than 3. Previous estimates ignored such a constraint and either focused on explaining all of the DIRBE excess (Santos et al. 2002; Salvaterra & Ferrara 2003) or amplitude of the measured near-IR background anisotropies (e.g., Fernandez et al. 2010).

In Figure 6, we show the total near-IR background intensity spectrum for different transition redshifts $z_{\rm t}$ from Pop II to Pop III stars with increasing redshift. Here, we take four transition redshifts $z_{\rm t} = 10$, 15, 20, and 30 using Equation (26). To maintain the same optical depth to electron scattering $\tau = 0.090$, we find a higher intensity is predicted for higher $z_{\rm t}$. Correspondingly f_* should be increased to values of 0.040, 0.043, and 0.044 for $z_{\rm t} = 15$, 20, and 30, respectively, compared to $f_* = 0.03$ for $z_{\rm t} = 10$. If $z_{\rm t} = 30$ (red dotted line) the integrated intensity is about ∼3–4 times greater than the case for $z_{\rm t} = 10$ (blue solid line) when $\lambda_{\rm obs} > 2\,\mu$m. Also, the peak of the integrated intensity spectrum moves to longer wavelengths as $z_{\rm t}$ is increased. This is because the Pop III stars are generally hotter than the Pop II stars, which can produce more ionizing photons. When the transition redshift is higher, the longer the Pop II stars dominate the universe, and less ionizing photons are produced when compared with the case for a low $z_{\rm t}$. To keep the reionization history unchanged, we need more Pop II stars to generate enough ionizing photons. This results in a near-IR background intensity that is higher.

7.2. Bright-end Galaxy Luminosity Functions

In order to relate our galaxy population responsible for reionization to the observations, we also compare our model

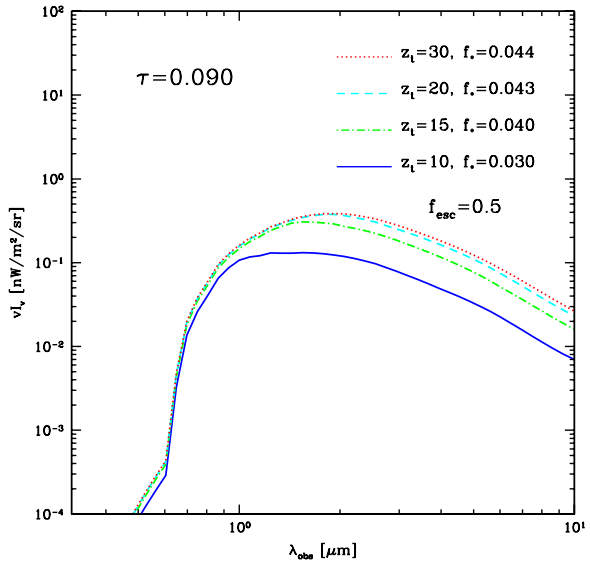

Figure 6. Total near-IR background intensity spectrum for transition redshifts z_t of Pop II and Pop III stars between 10 and 30. To maintain the same optical depth to electron scattering of $\tau = 0.090$, a higher intensity is predicted as z_t is increased. For example, the integrated intensity when $z_t = 30$ (red dotted line) is ∼3–4 times greater than when $z_t = 10$ (blue solid line) for $\lambda_{obs} > 2\ \mu$m.

(A color version of this figure is available in the online journal.)

to observations of $z > 6$ galaxies, focusing on the UV LFs. To obtain the UV LF, instead of the occupation number which is luminosity independent, we make use of the conditional luminosity function (CLF) approach (Yang et al. 2003; Cooray & Milosavljevic 2005; Cooray 2005). To compute the CLF, we map galaxy rest-frame UV luminosity to halo mass with some scatter added similar to the case of low-redshift galaxy populations (Cooray 2005). The total luminosity of a halo is taken to be

$$L_{\rm tot}(M, z) = l_\nu(z) f_* \frac{\Omega_{\rm b}}{\Omega_{\rm M}} M\,, \tag{49}$$

and we assume that this total luminosity can be ascribed to the central galaxy when $M_{\rm min} < M < M_{\rm sat}$, following the earlier description related to the occupation number. When $M > M_{\rm sat}$, we introduce satellites with central galaxy luminosity kept fixed at $L_{\rm tot}(M_{\rm sat}, z)$. However, when comparing to the existing measurements, we found that all of the rest-UV LF measurements are in the range where central galaxies dominate the LF and thus our comparison to the measured LFs is independent of assumptions related to the exact form of the satellite occupation number or CLF.

To compare with existing rest-UV LF measurements, we convert the luminosity of each galaxy to the AB absolute magnitude via the relation $M_{\rm AB} = -2.5\log_{10} L_\nu + 5.48$.[4] In the left panel of Figure 7, we show the SFRD as a function of redshift derived from Equation (25) for three reionization histories with $\tau = 0.077$, 0.090, and 0.099, which are obtained by setting $f_* = 0.02$, 0.03, and 0.04, respectively. The red points are the data from HUDF09+ERS+CANDELS observations (Bouwens et al. 2011). We find the SFRD of the three cases are higher than the existing measurements, especially at the high redshifts. This difference is mainly due to the fact that existing SFRD estimates are limited to galaxies with $M_{\rm UV} < -17$, while the bulk of the reionization UV density budget is contained in the galaxies at the faint end of the LF. This is especially the case at high redshift since the faint-end slope of the LF is steep with values reaching close to −2 already.

In the right panel of Figure 7, we show our rest-UV LF (corresponding to $\lambda_{\rm res} = 1600$ Å) at $z = 6$, 7, and 8. The central thick solid curves are the LF derived from our default model with

[4] http://www.ucolick.org/∼cnaw/sun.html

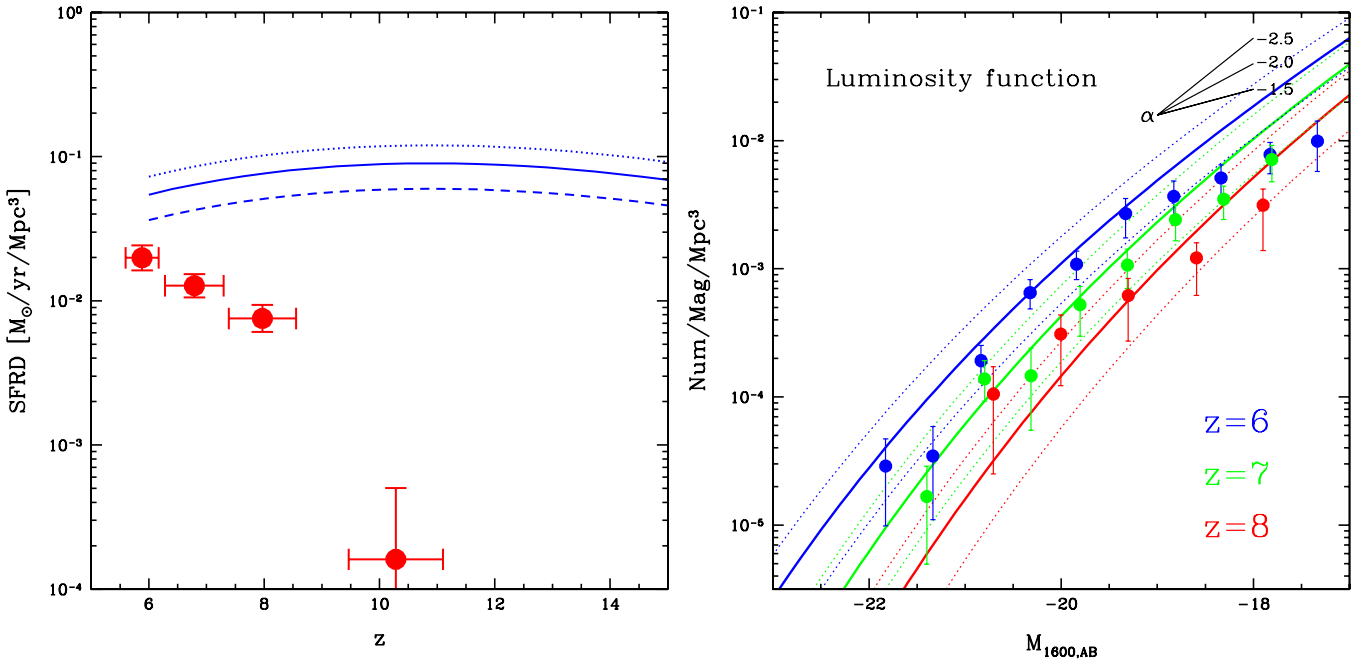

Figure 7. Left: the SFRD as a function of the redshift derived from Equation (25) for three reionization histories $\tau = 0.077$ (blue dashed line), 0.090 (blue solid line), and 0.099 (blue dotted line), which are obtained by setting $f_* = 0.02$, 0.03, and 0.04, respectively. The red points are the measurements from HUDF09+ERS+CANDELS observations (Bouwens et al. 2011). Right: the estimated UV luminosity function at $z = 6$, 7, and 8 with $\lambda_{\rm res} = 1600$ Å. The central thick solid lines are derived from our model with $f_* = 0.03$ at $z = 6$, 7, and 8, and the thin dotted lines are for $f_* = 0.04$ (upper) and 0.02 (lower), which can match the 1σ error of the data given in Bouwens et al. (2012). The faint-end slope α at three values are also shown in black solid lines for comparison.

(A color version of this figure is available in the online journal.)

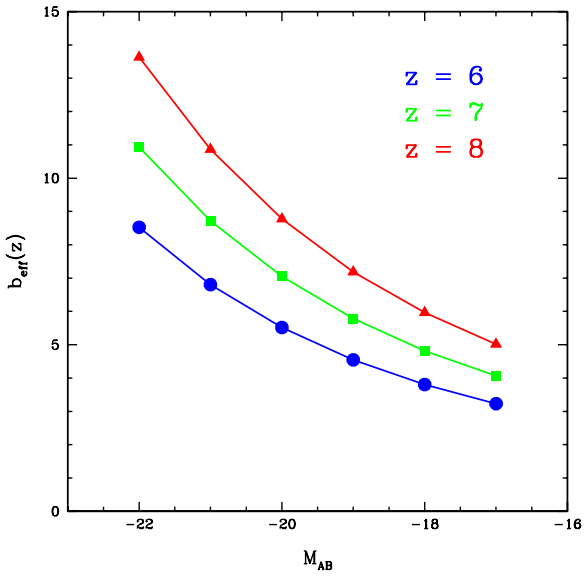

Figure 8. Effective galaxy bias vs. AB magnitude $M_{\rm AB}$ at $z = 6$, 7, and 8. We find the bias increases at higher redshifts and lower $M_{\rm AB}$.

(A color version of this figure is available in the online journal.)

$f_* = 0.03$ and $\tau = 0.090$, and the thin dotted lines are obtained by $f_* = 0.02$ (lower) and 0.04 (upper), which could match the 1σ errors of the data given in Bouwens et al. (2012). The three values of the faint-end slope $\alpha = -2.5$, -2.0, and -1.5 are shown, which indicates the slope of our model is between -2.5 and -2.0. Also, we find the star formation timescale $t_{\rm SF}$ is around 6×10^8 yr at $z = 6$, 7, and 8 when we calculate the luminosity mass function here.

We also explore the dependence of the galaxy bias on the $M_{\rm AB}$ in Figure 8. We can define a effective galaxy bias here from the HOD model as

$$b_{\rm eff}(z) = \int_{M_{\rm min}}^{M_{\rm max}} dM \frac{dn}{dM} b(M, z) \frac{\langle N_{\rm gal} \rangle}{\bar{n}_{\rm gal}} . \quad (50)$$

In the plot, we show the $b_{\rm eff}$ as a function of $M_{\rm AB}$ at z =6, 7, and 8 for the $M_{\rm AB} = -22$ to -17. We find that the galaxy bias increases as the redshift increases and decreases as the $M_{\rm AB}$ increases. The reason is obvious: The galaxy number density $\bar{n}_{\rm gal}$ defined by Equation (38) becomes smaller at higher redshift and bigger at larger $M_{\rm AB}$ (the larger $M_{\rm AB}$ means smaller halo mass M).

7.3. Anisotropy Power Spectrum

In Figure 9, we show the near-IR background anisotropy angular power spectrum at $\lambda_{\rm obs} = 3.6\,\mu$m. The clustering power spectra with nonlinear power spectrum from the HOD model are shown with solid lines. The left panel shows the case with $M_{\rm min}$, the minimum mass to host a galaxy, is changed from 10^6 to 10^9 $M_\odot$. For comparison, we also plot the linear power spectrum, which has a turnover around $\ell = 10^3$. When calculating the clustering power spectrum, we set the parameters of the HOD with $M_{\rm min}$ values as listed in the figure with $M_{\rm sat} = 15\,M_{\rm min}$. The corresponding values on the optical depth to electron scattering are also listed in the figure. We note that the shot-noise amplitude is larger for the case with $M_{\rm min} = 10^9\,M_\odot$ in comparison to the case with, say, $M_{\rm min} = 10^6\,M_\odot$, although in those two cases the clustering amplitude is higher with $M_{\rm min} = 10^6\,M_\odot$. This is because the shot-noise amplitude is sensitive to the second flux moment of the number counts. By keeping the minimum mass higher, we force the overall counts to be restricted to brighter sources than the case with a lower minimum halo mass. On the other hand, the clustering power spectrum reflects the total

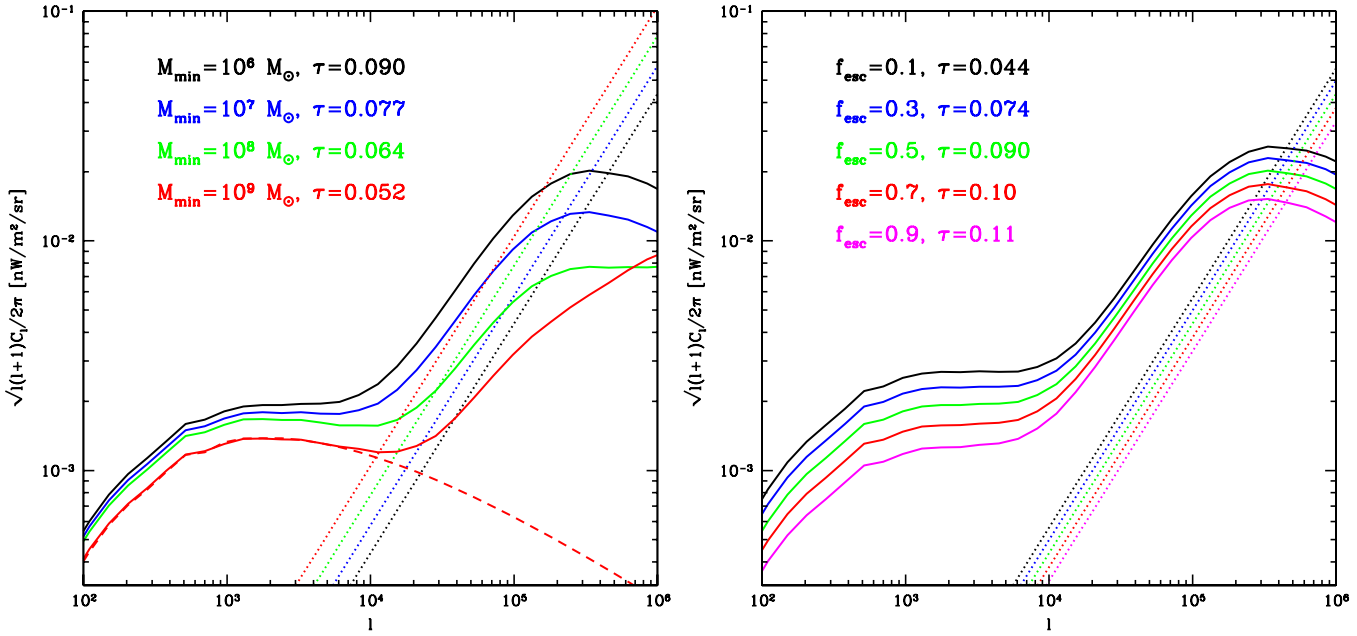

Figure 9. Near-IR background intensity anisotropy power spectrum at $\lambda_{\rm obs} = 3.6\,\mu$m. The solid lines are the total clustering power spectrum with the nonlinear power spectrum from the HOD model. Left: we show a variety of predictions with $M_{\rm min}$ related to the occupation number taken to be values shown in the plot. In all of these cases, we take $M_{\rm sat} = 15\,M_{\rm min}$. As $M_{\rm min}$ corresponds to the minimum halo mass to host a galaxy, the reionization history is also changed and we list the optical depth to electron scattering for the four cases we have studied here. For comparison, the linear power spectrum is shown as a dashed line for one of the cases, which has a turnover around $\ell = 10^3$ (Cooray et al. 2004). The shot-noise power spectra are shown with dotted lines. Note that the shot-noise level is higher when $M_{\rm min}$ is larger. Right: clustering predictions as a function of $f_{\rm esc}$. Note that the amplitude of the clustering power spectrum is higher with a smaller value for $f_{\rm esc}$. However, the optical depth to electron scattering is lower with a small value of $f_{\rm esc}$.

(A color version of this figure is available in the online journal.)

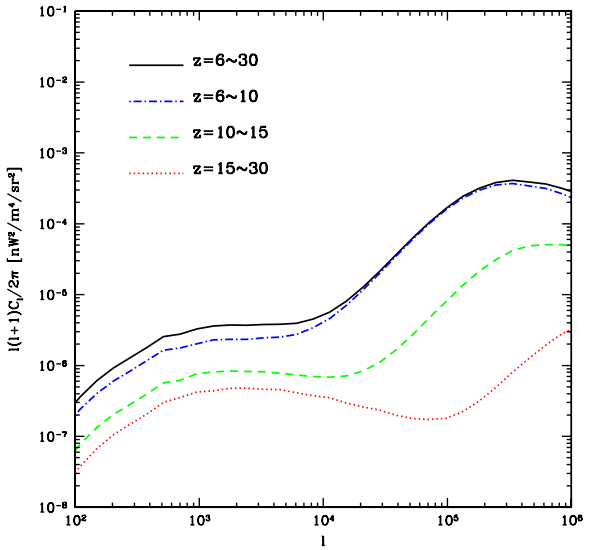

Figure 10. Angular power spectrum at 3.6 μm for different redshift bins. The power spectrum dominates over the redshift range of 6–10. The model shown here is the default case with $\tau = 0.090$ with $f_{\rm esc} = 0.5$ and $f_* = 0.03$.
(A color version of this figure is available in the online journal.)

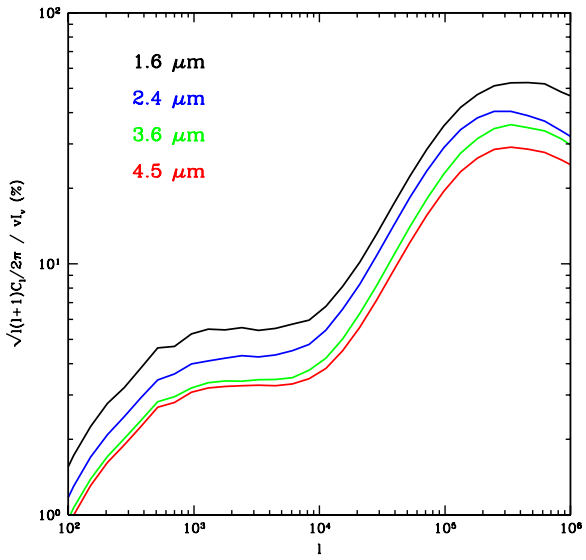

Figure 11. Ratio of rms fluctuations to the total intensity at different wavelengths $\lambda_{\rm obs} = 1.6$, 2.4, 3.6, and 4.5 μm. We find that the near-IR background fluctuations are around 10% compared with the background intensity from $\ell = 10^3$ to 10^4.
(A color version of this figure is available in the online journal.)

background intensity. With the minimum mass lowered, both the overall number density of galaxies and the background intensity are increased.

The right panel of Figure 9 shows the case where we vary $f_{\rm esc}$ to highlight the fact C_l amplitude is inversely proportional to $f_{\rm esc}^2$. However, one cannot arbitrarily reduce $f_{\rm esc}$ to a small value since this results in a low optical depth to electron scattering. If $M_{\rm min} \sim 10^8$ to 10^9, such that one does not need to be concerned with effects due to feedback negatively impacting the formation of galaxies in lower mass halos, then we find that $f_{\rm esc}$ must be at the level of 0.3 or more, under the assumptions related to the IMFs for Pop II and Pop III stars we use in this paper.

In Figure 10, we plot the C_ℓ at different redshift bins. As can be seen, the main contribution of the C_ℓ comes from the lowest redshift range of 6–10. For all practical purposes, one can assume that the near-IR background is probing the end of reionization not the first objects to form in the universe at the beginning of reionization.

To compare with the total near-IR intensity spectrum, we plot the ratio of the square root of C_ℓ to the νI_ν in Figure 11. We integrate from $z = 6$ to 30 with the same HOD model described above. For easy comparison, we restrict the predictions to be with $M_{\rm min} = 10^6\ M_\odot$ such that $\tau \sim 0.090$ to remain consistent with *WMAP* seven-year result. We find the ratio of $\sqrt{\ell(\ell+1)C_\ell/2\pi}$ to νI_ν is about 10% for $10^3 < \ell < 10^4$ and the clustering fluctuations amplitude is below 100% of the intensity at all angular scales. This shows that large fluctuations of the background intensity is not expected and the background behaves in a manner that is smooth and not clumpy as in the case if spatial variations are dominated by rare, bright galaxies.

In Figure 12, we show the near-IR background intensity power spectrum (solid curves), shot-noise power spectrum (dotted curves) with a comparison to existing observational measurements at several wavelengths: $\lambda_{\rm obs} = 1.6$, 2.4, 3.6, and 4.5 μm (Thompson et al. 2007; Matsumoto et al. 2011; Kashlinsky et al. 2012). Note that for the data from Kashlinsky et al. (2012) at 3.6 and 4.5 μm, we removed the IRAC beam transfer function B_ℓ so the comparison to theoretical predictions is easier. An accounting of the beam is essential since realistic instruments do not have perfect resolution, causing a loss of power on the smallest scales. This effect can be explicitly measured from the point-spread function. We calculate the beam transfer function B_ℓ by taking the power spectrum of the measured point-spread function for the *Spitzer*/IRAC instrument, which is publicly available and compute $C_\ell \rightarrow C_\ell/B_\ell$ (for more information see J. Smidt et al. 2012, in preparation).

We also show the results from the simulation in Fernandez et al. (2012) for comparison. The red solid and magenta dashed lines are for the simulation with mass resolution $M_{\rm min} = 10^8$ and $M_{\rm min} = 10^9\ M_\odot$, respectively. These two cases are described in their work as not having a suppression of the small mass halos (i.e., star formation present in halos with mass between 10^8 and $10^9\ M_\odot$, where one expects photoionization heating to suppress star formation). The reionization histories of these two cases involve Pop II stars with $f_{\rm esc} = 0.1$.

For more clarity, we show the square root of the C_ℓ at $\ell = 3 \times 10^3$ and $\ell = 10^4$ together with the data as a function of the wavelength in Figure 13. The data points are from the data sets shown in Figure 12, which are around $\ell = 3 \times 10^3$ or $\ell = 10^4$. We find the curve of the square root of the C_ℓ has similar shape to $\nu_{\rm obs} I_\nu$, but the amplitude of rms fluctuations in our models is lower than the existing measurements. We capture the uncertainties related to $f_*, f_{\rm esc}$, and $M_{\rm min}$ by considering a low and high range for our prediction related to C_l with τ falling within the 1σ uncertainty range of the *WMAP* seven-year result when these parameters are varied. Even with parameter uncertainties accounted for, we find that the existing measurements are at least an order of magnitude larger than our model predictions.

We attempted additional model variations but failed to find a scenario where τ is consistent with *WMAP* seven-year result and the existing LFs leading to a model consistent with existing near-IR background. One can, in principle, model fit the near-IR fluctuation power spectra by increasing the photon output of first galaxies. This results in an optical depth that is higher than the *WMAP* value and an LF that has brighter galaxies than observed in existing deep *HST*/WFC3 images. The

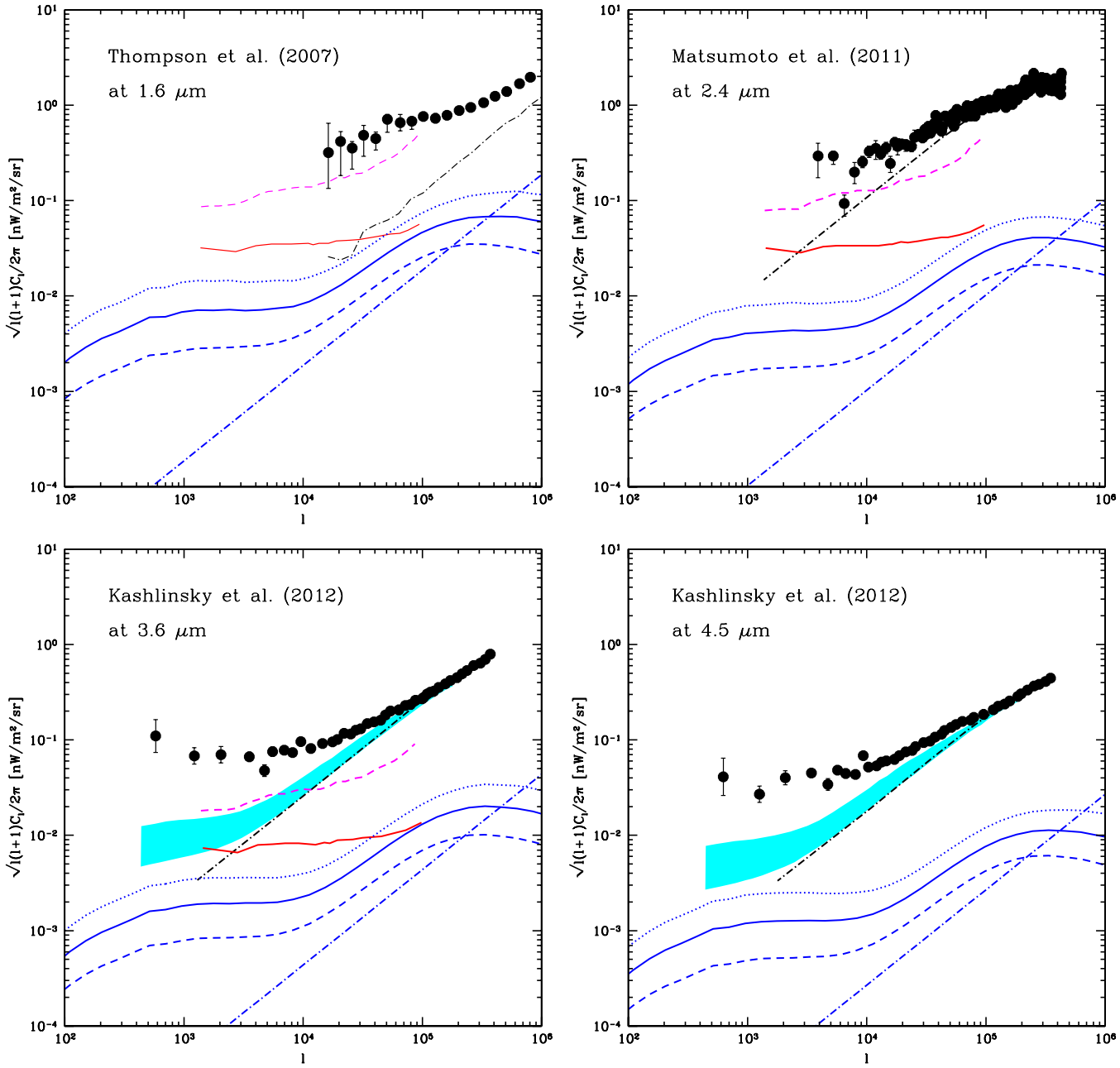

Figure 12. Comparison of our C_ℓ with the current measurements at different wavelengths. The clustering power spectra are in blue solid ($f_* = 0.03$ and $f_{\rm esc} = 0.5$), dashed ($f_* = 0.02$ and $f_{\rm esc} = 0.9$), and dotted ($f_* = 0.04$ and $f_{\rm esc} = 0.1$) lines with $M_{\rm min} = 10^6\ M_\odot$ in our HOD model. The shot-noise power spectrum is shown as blue dash-dotted lines. The observational data of shot noise are shown as black dash-dotted lines. For the data of Kashlinsky et al. (2012) at 3.6 and 4.5 μm, we removed the beam function so that a direct comparison can be made to model predictions. The simulation results from Fernandez et al. (2012) are also shown with minimum halo mass set at $M_{\rm min} = 10^8$ (lower red solid) and $M_{\rm min} = 10^9\ M_\odot$ (upper magenta dashed), without a suppression related to the star formation in halos between the range of 10^8 and $10^9\ M_\odot$ where photoionization effects become important. The shaped region in each of the two lower panels is an estimate of the residual anisotropy power spectrum signal expected from low-redshift faint galaxies following Helgason et al. (2012). These two curves clearly show the presence of excess clustering at $\ell \sim 10^3$. While this excess has been suggested as originating from reionization (Kashlinsky et al. 2012), we do not find this to be the case as our predictions are lower.

(A color version of this figure is available in the online journal.)

existing measurements require a background intensity that is at least 3 nW m^{-2} sr^{-1} at 1.6 μm so that the model predictions become consistent with measurements within the 1σ uncertainties of the measurements. Since 0.3 nW m^{-2} sr^{-1} at 1.6 μm is associated with 2.5 H-ionizing photons per baryon during reionization, if reionization is to explain the background fluctuations then we are dealing with a situation where $\sim$25 H-ionizing photons per baryon are present. A possibility is to introduce a spectrum for the emission that has a rest-frame cutoff in UV at wavelengths shortward of the Lyman limit that is not associated with reionization but by the emission mechanism itself. Unfortunately, we have not been able to come up with such an emission spectrum.

As discussed in Helgason et al. (2012) faint, low-redshift galaxies do not have a clustering shape consistent with the anisotropy power spectrum measurements. The existing measurements show a clear excess in clustering at 30 arcsec to few tens arcminute angular scales that differ from faint galaxy

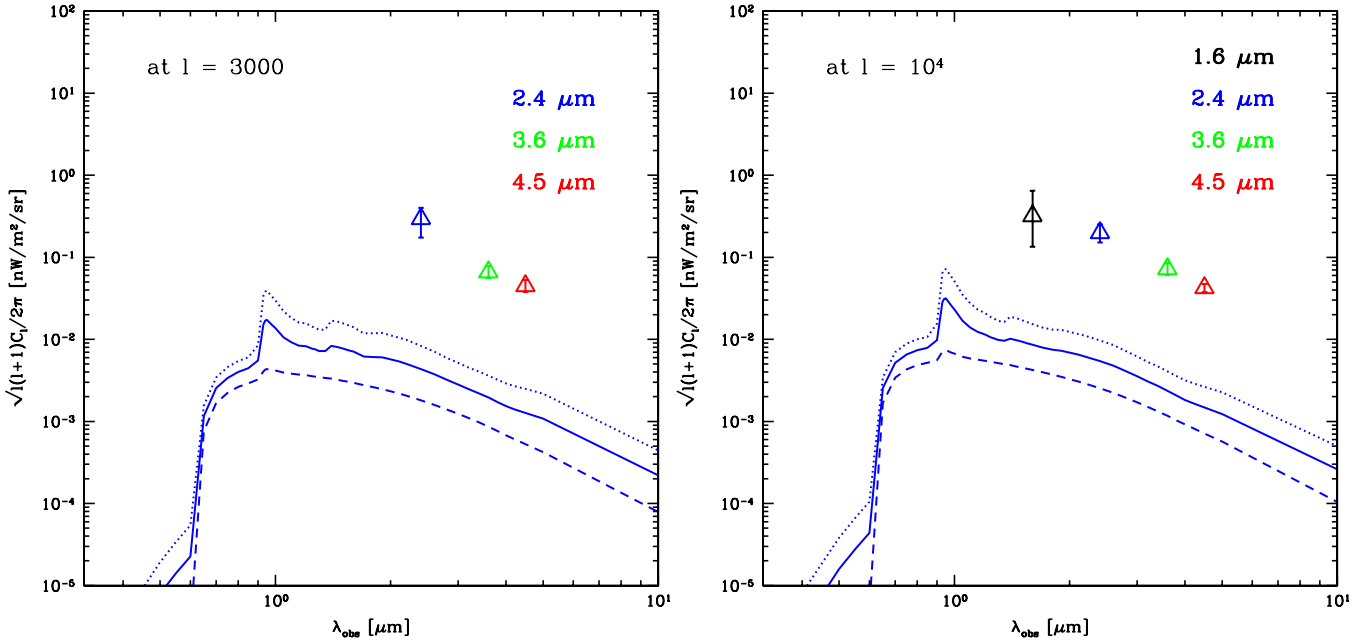

Figure 13. Square root of the C_ℓ at $\ell = 3 \times 10^3$ and $\ell = 10^4$ compared to the observational data at different wavelengths $\lambda_{\rm obs} = 1.6$, 2.4, 3.6, and 4.5 μm. The blue solid, dashed, and dotted lines are the square root of the C_ℓ with $f_* = 0.03$ and $f_{\rm esc} = 0.5$, $f_* = 0.02$ and $f_{\rm esc} = 0.9$, and $f_* = 0.04$ and $f_{\rm esc} = 0.1$, respectively. The data points are from the data sets shown in Figure 12 around $\ell = 3 \times 10^3$ or $\ell = 10^4$.

(A color version of this figure is available in the online journal.)

clustering power spectrum. This difference is statistically significant and one can only explain at most 20% of the near-IR fluctuations to be associated with faint galaxies, reducing the previous estimate in Cooray et al. (2007; Chary et al. 2008) that suggested a contribution at the 50% level. We are now left with an unexplained set of measurements since neither the low-redshift faint galaxies nor the high-redshift reionization galaxies can explain them. One possibility is that the existing fluctuation excess in the data has a non-astrophysical origin, perhaps either involving systematics in the data or fluctuations in the zodiacal light. While arguments have been made that these effects are insignificant, with a set of well-coordinated multi-wavelength measurements we plan to further address the origin of near-IR fluctuations in our upcoming papers.

8. SUMMARY

The UV emission from stars which are formed in the early universe from $z = 6$ to 30 can contribute to the near-IR background light. By measuring the intensity and anisotropies of the near-IR background, we can investigate the properties of these early stars and the epoch of reionization. In this work, we discuss several sources that contribute to the near-IR background intensity, including the emission of stars, Lyα, free–free, free–bound, and two photon. We first estimate the frequency spectrum separately for Pop II and Pop III stars with the redshift range $z = 6$–30. By using the initial stellar mass spectrum and the fitting model of time-averaged hydrogen photoionization rate, we calculate the luminosity mass density. We find that although the luminosity mass density of the Pop III stars is a bit larger than that of Pop II stars, the near-IR intensity spectrum from the Pop II stars is stronger than that from Pop III stars, which is caused by the longer lifetime of Pop II stars.

In order to check the consistence of our stellar model and the reionization history, we derive the hydrogen reionization fraction at different redshifts and calculate the optical depth by assuming that the Pop II stars are dominant for $z \lesssim 10$ while Pop III stars for $z \gtrsim 10$. We find that if we set the star formation efficiency $f_* = 0.03$, the universe would be totally reionized around $z = 9$ with the optical depth $\tau = 0.090$, which is well consistent with the result from the *WMAP* seven-year data. Also, we explore the other possible models with $f_* = 0.02$ and 0.04 and get $\tau = 0.077$ and 0.099, respectively. The total number of the ionizing photon per baryon required to maintain the ionized IGM, $N^p_{\rm ion}(z)$, is also evaluated for the three cases, and we find the $N^p_{\rm ion}(z)$ becomes a constant with a value around 2.5 after $z = 15$.

To compare with existing bright-end LF measurements, we evaluate the UV LF from our model at $\lambda_{\rm res} = 1600$ Å for $z = 6$, 7, and 8 from $M_{\rm AB} = -22$ to -17. We compare to the measurements of Bouwens et al. (2012). We find our derived LF is consistent with the data with the slope of the faint-end $\alpha \sim -2$. This is a steep slope and existing measurements do suggest that the slope is steeper than for LFs at low redshifts. We then define an effective galaxy bias $b_{\rm eff}$ from the HOD model, and find the $b_{\rm eff}$ becomes bigger at high redshift and bright luminosities because of the lower number density of the galaxies.

Finally, we calculate the angular power spectrum of the near-IR background by making use of a halo model. The nonlinearities provided by the one-halo term increase the clustering strength at multipoles greater than about $\ell \sim 2 \times 10^3$. The suggested turnover at this scale with the linear power spectrum alone in Cooray et al. (2004) is no longer present. We find that the shot-noise power spectrum of the Pop III stars is greater than that of Pop II stars because of the larger luminosity mass density for Pop III stars. By making use of the stellar population evolution model, we calculate the near-IR anisotropy power spectra C^ν_ℓ at different wavelengths and compare to the observational data. We find that our results are lower than the observational data by at least an order of magnitude. There are now strong arguments that the near-IR anisotropies cannot originate from low-redshift faint galaxies (Helgason et al. 2012). We have failed to ex-

plain the alternative origin of near-IR background anisotropies involving galaxies present during reionization, contrary to suggestions in the literature (Kashlinsky et al. 2012). In future works, using additional measurements with *Spitzer* and *Hubble*/WFC3, we plan to further discuss the near-IR fluctuations and to explain if the origin is astrophysical or whether it is associated with yet-unknown systematic effect in the data.

This work was supported by NSF CAREER AST-0645427 and NASA NNX10AD42G at UCI. We thank CIBER, SDWFS, and CANDELS teams for helpful discussions and questions that motivated this paper.

REFERENCES

Bernstein, J., & Dyson, F. 2003, PASP, 115, 1383
Bock, J., Battle, J., Cooray, A., et al. 2006, New Astron. Rev., 50, 215
Bock, J., Sullivan, I., Arai, T., et al. 2012, arXiv:1206.4702
Bouwens, R. J., Illingworth, G. D., Oesch, P. A., et al. 2011, ApJ, 737, 90
Bouwens, R. J., Illingworth, G. D., Oesch, P. A., et al. 2012, ApJ, 752, L5
Brown, R. L., & Mathews, W. G. 1970, ApJ, 160, 939
Cambrésy, L., Reach, W. T., Beichman, C. A., & Jarrett, T. H. 2001, ApJ, 555, 563
Cantalupo, S., Porciani, C., & Lilly, S. J. 2008, ApJ, 672, 48
Chary, R., Cocray, A., & Sullivan, I. 2008, ApJ, 681, 53
Cooray, A. 2005, MNRAS, 365, 842
Cooray, A., Bock, J., Kawada, M., et al. 2009, in ASP Conf. Ser. 418, AKARI: A Light to Illuminate the Misty Universe, ed. T. Onaka et al. (San Francisco, CA: ASP), 535
Cooray, A., Bock, J. J., Keatin, B., Lange, A. E., & Matsumoto, T. 2004, ApJ, 606, 611
Cooray, A., & Milosavljevic, M. 2005, ApJ, 627, L89
Cooray, A., & Sheth, R. 2002, Phys. Rep., 372, 1
Cooray, A., Sullivan, I., Chary, R., et al. 2007, ApJ, 659, L91
Cooray, A., & Yoshida, N. 2004, MNRAS, 351, L71
Dopita, M. A., & Sutherland, R. S. 2002, Astrophysics of the Diffuse Universe (New York: Springer)
Eisenstein, D. J., & Hu, W. 1997, ApJ, 496, 605
Fernandez, E., & Komatsu, E. 2006, ApJ, 646, 703
Fernandez, E. R., Iliev, I. T., Komatsu, E., & Shapiro, P. R. 2012, ApJ, 750, 20
Fernandez, E. R., Komatsu, E., Iliev, I. T., & Shapiro, P. R. 2010, ApJ, 710, 1089
Giovanardi, C., Natta, A., & Palla, F. 1987, A&AS, 70, 269
Grogin, N., Kocevski, D. D., Faber, S. M., et al. 2011, ApJS, 197, 35
Helgason, K., Ricotti, M., & Kashlinsky, A. 2012, ApJ, 752, 113
Hummer, D. G. 1994, MNRAS, 268, 109
Kashlinsky, A., Arendt, R. G., Ashby, M. L. N., et al. 2012, ApJ, 753, 63
Kashlinsky, A., Arendt, R., Gardner, J. P., Mather, J. C., & Moseley, S. H. 2004, ApJ, 608, 1
Kashlinsky, A., Arendt, R. G., Mather, J., & Moseley, S. H. 2005, Nature, 438, 45
Kashlinsky, A., Arendt, R. G., Mather, J., & Moseley, S. H. 2007, ApJ, 654, L5
Koekemoer, A., Faber, S. M., Ferguson, H. C., et al. 2011, ApJS, 197, 36
Komatsu, E., Smith, K. M., Dunkley, J., et al. 2011, ApJS, 192, 18
Kuhlen, M., & Faucher-Giguere, C. 2012, MNRAS, 423, 862
Larson, R. B. 1998, MNRAS, 301, 569
Larzas, W. J., & Latter, R. 1961, ApJS, 6, 167
Lejeune, T., & Schaerer, D. 2001, A&A, 336, 538
Loeb, A., & Rybicki, G. B. 1999, ApJ, 524, 527
Madau, P., & Pozzetti, L. 2000, MNRAS, 312, 9
Madau, P., Pozzetti, L., & Dickinson, M. 1998, ApJ, 498, 106
Madau, P., & Silk, J. 2005, MNRAS, 359, L37
Matsumoto, T., Seo, H. J., Jeong, W.-S., et al. 2011, ApJ, 742, 124
Navarro, J. F., Frenk, C. S., & White, S. D. M. 1995, ApJ, 462, 563
Raue, M., Kneiske, T., & Mazin, D. 2009, A&A, 498, 25
Salpeter, E. E. 1955, ApJ, 121, 161
Salvaterra, R., & Ferrara, A. 2003, MNRAS, 339, 973
Santos, M. R., Bromm, V., & Kamionkowski, M. 2002, MNRAS, 336, 1082
Seager, S., Sasselov, D. D., & Scott, D. 1999, ApJ, 523, L1
Schaerer, D. 2002, A&A, 382, 28
Sheth, R. K., & Tormen, G. 1999, MNRAS, 308, 119
Shull, J. M., Harness, A., & Trenti, M. 2011, arXiv:1108.3334
Thompson, R. I., Eisenstein, D., Fan, X., Rieke, M., & Kennicutt, R. C. 2007, ApJ, 657, 669
Totani, T., Yoshii, Y., Maihara, T., Iwamuro, F., & Motohara, K. 2001, ApJ, 559, 592
Trac, H., & Cen, R. 2007, ApJ, 671, 1
Yang, X., Mo, H. J., & van den Bosch, F. C. 2003, MNRAS, 339, 1057
Zheng, Z., Berlind, A. A., Weinberg, D. H., et al. 2005, ApJ, 633, 791